Climate, variability, and climate sensitivity of "Middle Atmosphere" chemistry configurations of the Community Earth System Model Version 2, Whole Atmosphere Community Climate Model Version 6 (CESM2(WACCM6))

N. A. Davis[1], D. Visioni[2], R. R. Garcia[1], D. E. Kinnison[1], D. R. Marsh[3], M. Mills[1], J. H. Richter[3], S. Tilmes[1], C. G. Bardeen[1], A. Gettelman [4], A. A. Glanville[3], D. G. MacMartin[2], A. K. Smith[1], F. Vitt[1,5]

[1]Atmospheric Chemistry and Modeling Observations Laboratory, National Center for Atmospheric Research, Boulder, CO, USA

[2]Sibley School of Mechanical and Aerospace Engineering, Cornell University, Ithaca, NY, USA

[3]Climate and Global Dynamics Laboratory, National Center for Atmospheric Research, Boulder, CO, USA

[4]Pacific Northwest National Laboratory, Richland, WA, USA

[5]High Altitude Observatory, National Center for Atmospheric Research, Boulder, CO, USA

Key Points:

- There are differences in stratospheric aerosol optical depth between comprehensive and simplified middle atmosphere chemistry configurations
- Simplifying the chemistry scheme generally has smaller global impacts than coarsening the horizontal resolution
- All configurations have similar climate sensitivities and responses to forcings

Corresponding author: N. A. Davis, nadavis@ucar.edu

Abstract

Simulating whole atmosphere dynamics, chemistry, and physics is computationally expensive. It can require high vertical resolution throughout the middle and upper atmosphere, as well as a comprehensive chemistry and aerosol scheme coupled to radiation physics. An unintentional outcome of the development of one of the most sophisticated and hence computationally expensive model configurations is that it often excludes a broad community of users with limited computational resources. Here, we analyze two configurations of the Community Earth System Model Version 2, Whole Atmosphere Community Climate Model Version 6 (CESM2(WACCM6)) with simplified "middle atmosphere" chemistry at nominal 1 and 2 degree horizontal resolutions. Using observations, a reanalysis, and direct model comparisons, we find that these configurations generally reproduce the climate, variability, and climate sensitivity of the 1 degree nominal horizontal resolution configuration with comprehensive chemistry. While the background stratospheric aerosol optical depth is elevated in the middle atmosphere configurations as compared to the comprehensive chemistry configuration, it is comparable between all configurations during volcanic eruptions. For any purposes other than those needing an accurate representation of tropospheric organic chemistry and secondary organic aerosols, these simplified chemistry configurations deliver reliable simulations of the whole atmosphere that require 35% to 86% fewer computational resources at nominal 1 and 2 degree horizontal resolution, respectively.

Plain Language Summary

Modeling the entire atmosphere, from the surface to an altitude of 140 kilometers (87 miles), and all of its unique physics takes a lot of computer resources. There are many people who would like to simulate the whole atmosphere to study climate change, space weather, and extreme events, but they can't because these models have become too computationally expensive to run. We examined a whole atmosphere model with a simpler chemistry scheme, and at a lower horizontal resolution, to see if it still reproduces major features of climate and climate change. The two configurations perform similarly to the high resolution simulation with complex chemistry, with some minor and understandable differences. Anyone looking to simulate the whole atmosphere, using fewer computational resources, can do so confidently using the described model configurations, as long as they are aware of some of the deficiencies.

1 Introduction

Whole atmosphere climate models resolve the interactions between atmospheric dynamics, chemistry, aerosols, and upper atmosphere physics, and are needed to study a wide range of scientific problems. This includes: stratospheric ozone loss (Solomon et al., 1986; Solomon, 1999), its recovery (Fang et al., 2019), and the potential limits of recovery due to future aircraft (J. Zhang et al., 2021) and wildfire emissions (Solomon et al., 2022); geoengineering intended to offset greenhouse gas-induced warming (National Academies of Sciences, Engineering, and Medicine, 2021; Kravitz et al., 2015; Tilmes et al., 2020; Visioni et al., 2021; Weisenstein et al., 2022) and its side effects (Visioni et al., 2020; Tilmes et al., 2021, 2022); sudden stratospheric warming impacts on upper atmosphere variability (Baldwin et al., 2021; Pedatella et al., 2021); space weather (Sinnhuber et al., 2012; Damiani et al., 2016; Sinnhuber et al., 2018; Meraner & Schmidt, 2018) and meteor (Plane, 2012) impacts on stratospheric ozone; and the acceleration of the Brewer-Dobson circulation (Abalos et al., 2019; Polvani et al., 2019; Chrysanthou et al., 2020; Abalos et al., 2021), its potential impacts on stratospheric (Butchart & Scaife, 2001; Maliniemi et al., 2021) and tropospheric ozone (Neu et al., 2014), and its implications for global volcanic aerosol transport (Aubry et al., 2021).

These problems have motivated the development of the Community Earth System Model Version 2, Whole Atmosphere Community Climate Model Version 6 (CESM2(WACCM6)), a state of the art fully-coupled whole atmosphere chemistry-climate model with a domain that extends from the surface to the lower thermosphere. The configuration with comprehensive troposphere-stratosphere-mesosphere-lower thermosphere ("TSMLT") chemistry (Emmons et al., 2020) at nominal 1 degree horizontal resolution was evaluated by Gettelman, Mills, et al. (2019). However, its computational cost is prohibitive to many researchers and for certain applications, such as long climate integrations.

While simulating the whole atmosphere requires comprehensive treatments of middle and upper atmosphere physics, including ion chemistry (Verronen et al., 2016) and energetic particle precipitation (Andersson et al., 2016), gravity wave transport (Garcia & Solomon, 1985; Garcia et al., 2017), and molecular diffusion (Chabrillat et al., 2002; Smith et al., 2011; Garcia et al., 2014), the elevated computational cost is primarily due to the inclusion of interactive whole atmosphere chemistry and aerosols. We present here two simpler configurations of CESM2(WACCM6) (Table 1) that make use of the sim-

Table 1. Approximate number of central processor unit (CPU) core hours needed to complete one simulated year of the specified configuration of CESM2(WACCM6), and approximate number of simulated years per day. All configurations assume interactive ocean, sea ice, and land model components. A core hour is the computational resource of running one CPU for one hour. 1 degree configurations were run with 3,564 cores, while the 2 degree configuration was run with 576 cores due to the inherent scaling limit of the finite volume dynamical core.

Configuration	Core hours	Throughput (sim. year/day)
1 deg., TSMLT	19,900	4.3
1 deg., MA	12,800	6.7
2 deg., MA	2,700	5.1

plified middle atmosphere ("MA") chemistry scheme, at both nominal 1 degree and nominal 2 degree horizontal resolutions. These configurations require 35% and 86% fewer computational resources, respectively, compared to the TSMLT configuration at a nominal 1 degree resolution. The MA scheme neglects non-methane hydrocarbon species and reactions that may otherwise be important for simulating the chemical composition of the troposphere (Kinnison et al., 2007). An important difference, though, is that the MA scheme produces a higher background stratospheric aerosol optical depth, in part due to the design of the modal aerosol scheme (Visioni et al., 2022).

Here we describe in detail the climate and variability of the middle and upper atmosphere, with a focus on zonal mean temperature and zonal mean zonal wind, sudden stratospheric warmings (SSWs), the Quasi-Biennial Oscillation (QBO), tropical stratospheric upwelling, and the tropical tape recorder, as well as several measures of surface climate, including global mean surface temperature, Arctic sea ice, and climate sensitivity. We show that many aspects of surface climate and middle atmospheric climate and variability are similar in these lower-cost configurations. With a few caveats, they can be used in studies that do not require all of the complexities of the comprehensive TSMLT configuration.

2 Model configurations

Our analysis focuses on configurations of CESM2(WACCM6) that use the finite volume dynamical core (Lin & Rood, 1997), with 70 vertical levels from the surface to 4.5×10^{-6} hPa - approximately 140 km altitude. The finite volume dynamical core is run at either a 1 degree nominal ($0.95°\times 1.25°$) or 2 degree nominal ($1.95°\times 2.25°$) horizontal resolution.

CESM2(WACCM6) inherits the physics of the low-top Community Atmosphere Model Version 6.0, including: Zhang-McFarlane deep convection (G. J. Zhang & McFarlane, 1995); Cloud Layers Unified By Binormals (Golaz et al., 2002; Larson, 2017), a unified turbulence and cloud scheme; Morrison-Gettelman Version 2 microphysics (Gettelman & Morrison, 2015); subgrid orographic drag (Beljaars et al., 2004); an orographic gravity wave scheme based on Scinocca and McFarlane (2000); the Rapid Radiative Transfer Model for General circulation models radiation (Mlawer et al., 1997; Iacono et al., 2008); and the Modal Aerosol Model Version 4 (Liu et al., 2016; Mills et al., 2016).

In addition to these shared physics schemes, CESM2(WACCM6) also includes convectively- and frontally-generated gravity wave schemes (Richter et al., 2010), molecular diffusion (Garcia et al., 2007), resolved gas-phase and aerosol chemistry, and photoionization, photodissociation, and photoelectron production by solar and geomagnetic forcings. The TSMLT (Gettelman, Mills, et al., 2019; Emmons et al., 2020) and MA (Kinnison et al., 2007) chemical mechanisms model the extended O_x, NO_x, HO_x, ClO_x, and BrO_x chemical families, CH_4 and its degradation products, N_2O, H_2O, CO_2, CO, and ClO_x and BrO_x precursors. The TSMLT mechanism also models nonmethane hydrocarbons, oxygenated organics, two very short-lived halogens, and secondary organic aerosols via the volatility basis set approach (Hodzic et al., 2016; Tilmes et al., 2019). The TSMLT mechanism includes a total of 231 species, 403 gas-phase reactions, and 30 heterogeneous reactions, while the MA mechanism includes a total of 59 species, 217 gas-phase reactions, and 17 heterogeneous reactions.

Surface area density derived from MAM4 is used to drive heterogeneous chemistry (Mills et al., 2016). Tropospheric heterogeneous reactions consider sulfate, black carbon, particulate organic matter, and secondary organic aerosol, while stratospheric heterogeneous reactions consider sulfate, nitric acid trihydrate, and water-ice (Mills et al., 2016,

2017; Gettelman, Mills, et al., 2019). A more complete description of the chemistry and aerosol suite can be found in Section 2.4 of Gettelman, Mills, et al. (2019).

WACCM6 is coupled to the Parallel Ocean Program Version 2 (POP2) (Danabasoglu et al., 2012), the Community Ice CodE Version 5 (CICE5) (Hunke et al., 2015), the Community Land Model Version 5 (CLM5) (Lawrence et al., 2019), and the Model for Scale Adaptive River Transport (MOSART) (Li et al., 2013) via the Community Infrastructure for Modeling Earth (CIME) coupler (Danabasoglu et al., 2020). POP2 is a comprehensive ocean model discretized onto 60 vertical levels and a "Greenland pole" horizontal mesh. POP2 includes parameterized ocean biogeochemistry. CICE5, a prognostic sea ice model, shares the same horizontal grid as POP2. Soil and vegetation dynamics and land surface biogeochemistry are modeled with CLM5, while river transport is modeled with MOSART.

Surface mixing ratios for greenhouse gases, reactive gases, and aerosols from anthropogenic sources and biomass burning are specified, while biogenic emissions from CLM5 and NO_x production by lightning are interactive and computed online. Volcanic emissions of SO_2 are prescribed from Volcanic Emissions for Earth System Models (Neely III & Schmidt, 2016) with modifications described in Mills et al. (2016).

The QBO is driven spontaneously by a mix of resolved tropical waves and parameterized gravity wave drag in both 1 degree configurations of the model. The 70 vertical levels in these simulations are insufficient to accurately resolve wave dissipation and the descent of the QBO, though this can be ameliorated by increasing the number of vertical levels to 110 (Garcia & Richter, 2019). However, the tropical zonal winds are nudged to observations between 4 and 86 hPa in the MA 2° configuration as it was not tuned to have a spontaneous QBO.

We conducted three Coupled Model Intercomparison Project Phase 6 (CMIP6) experiments: three Historical (HIST) simulation ensemble members, from 1850-2014; one preindustrial control (piControl) simulation from arbitrary years 0-1000; and one abrupt quadrupling of CO_2 ($4xCO_2$) simulation from arbitrary years 0-150 (Eyring et al., 2016), for each configuration. While 150 years is sufficient to obtain an estimate of climate sensitivity, it is likely to be an underestimate (Rugenstein et al., 2020). We also conducted one SSP2-4.5 simulation for the TSMLT and MA configurations to evaluate the mech-

anisms' stratospheric ozone recovery. All simulations are fully coupled, with prognostic ocean, sea ice, land, and river runoff components.

3 Evaluation datasets

We evaluate the zonal mean climate of the whole atmosphere using a combination of Modern Era Retrospective Reanalysis version 2 (MERRA2; Gelaro et al. (2017)) output and National Aeronautics and Space Administration (NASA) Sounding of the Atmosphere using Broadband Radiometry version 2.0 (SABER; Remsberg et al. (2008); Dawkins et al. (2018)) retrievals, in addition to NASA Microwave Limb Sounder version 4.2 (MLS; Lambert et al. (2007)) and NASA Solar Backscatter Ultraviolet (SBUV; McPeters et al. (2013)) satellite retrievals.

MERRA2 is a reanalysis that assimilates in-situ and remotely-sensed observations of the atmosphere to produce a highly-constrained reconstruction of atmospheric variability from 1980 to the present. Here we use temperature and zonal wind output from the assimilation product through 2014 (Global Modeling and Assimilation Office (GMAO), 2015). SABER, an instrument onboard the NASA Thermosphere Ionosphere Mesosphere Energetics and Dynamics (TIMED) satellite, makes limb measurements of CO_2, O_3, and H_2O infrared emissions, with temperature and geopotential retrievals available between approximately 100 and 0.0001 hPa.

While MERRA2 has a model lid at 0.01 hPa (Molod et al., 2015), its sponge layer begins at 0.24 hPa (Fujiwara et al., 2017). For this reason, we create a combined "MERRA2 & SABER" evaluation dataset that combines MERRA2 from the surface to 0.24 hPa, and SABER from 0.24 to 0.0001 hPa. In zonal mean plots, we leave the altitude regions between 0.24 hPa and 0.1 hPa shaded grey to note this transition. SABER only has continuous coverage between 53°S and 53°N (Randel et al., 2016), so we exclude all SABER retrievals poleward of 53° and similarly shade them grey. For SABER, daily average temperature and geopotential are gridded by interpolating each profile to a common pressure grid and then averaging into 1 degree zonal mean bins. Daily mean zonal winds are derived from gridded SABER geopotential through geostrophic balance. Monthly means are constructed by averaging these daily means.

MLS version 4.2 retrievals of water vapor are used as an evaluation dataset for the stratospheric tape recorder (Mote et al., 1996). MLS is situated onboard NASA's Earth

Observing System Aura satellite and measures microwave emissions from the atmospheric limb. As in Glanville and Birner (2017), daily profiles of water vapor are averaged between 10°S and 10°N to produce daily average stratospheric water vapor, from which monthly averages are constructed.

We use SBUV Version 8.6 merged ozone retrievals to evaluate polar stratospheric ozone. The merged dataset is constructed from ozone retrievals from nine satellites from 1970 to the present, including the Nimbus-4 BUV, Nimbus-7 SBUV, and NOAA SBUV/2 instruments. Excepting Nimbus-4, there is overlap among the different missions which allows for a more direct calibration, which presents some additional uncertainty for retrievals from 1970 to 1972.

Global mean surface temperatures are evaluated with two observational datasets: Goddard Institute for Space Studies Surface Temperature version 4 (GISSTEMPv4; Lenssen et al. (2019)) and Hadley Centre/Climatic Research Unit Temperature version 5 (HadCRUT5; Morice et al. (2012)). Both datasets combine observations of sea surface temperatures and air temperatures over land, with slightly different homogenization and hole-filling methods. We also evaluate Arctic sea ice with two observational datasets: sea ice area derived from the National Snow and Ice Data Center Sea Ice Index version 3 (NSIDC; Fetterer et al. (2017)), and sea ice volume from the Pan-Arctic Ice Ocean Modeling and Assimilation System (PIOMAS; Schweiger et al. (2011)). NSIDC is a fully observational product derived from passive microwave satellite measurements, while PIOMAS sea ice volume is derived from a sea ice model that assimilates satellite and in situ measurements (J. Zhang & Rothrock, 2003).

4 Methods and definitions

Following the World Meteorological Organization, the tropopause is defined as the first level at which the tropospheric lapse rate decreases to 2 K/km, provided it remains below 2 K/km between that level and all levels within 2 km above. We define the stratopause as the warmest level between the tropopause and 0.01 hPa, and the mesopause as the coldest level above the stratopause. The "pauses" are evaluated with monthly mean, zonal mean output.

SSWs are identified as in Charlton and Polvani (2007), which classifies the central date of an SSW as the date when the daily average zonal mean zonal wind at 10 hPa

and 60°N becomes easterly from November through March. After an SSW is identified, subsequent events are identified only if the central date occurs more than 20 days after the central date of the preceding event.

Tropical stratospheric upwelling, M, is defined as the area average of all transformed Eulerian mean (TEM) upward motion at each vertical level,

$$M(p) = 2\pi \int_{-90}^{90} [w^*](p,\phi)\delta(p,\phi)a\cos(\phi)d\phi \tag{1}$$

where a is the radius of the earth, p is the pressure, ϕ is the latitude, $[w^*]$ is the TEM residual vertical velocity, defined by

$$[w^*] = [w] + \frac{1}{a}\frac{\partial}{\partial\phi}\frac{[v'\theta']}{\partial[\theta]/\partial p} \tag{2}$$

where w is the vertical wind, θ is the potential temperature, brackets indicate the zonal mean, and primes indicate zonal deviations, and $\delta(p,\phi)$ is equal to 1 for positive $[w^*]$ and 0 otherwise.

Climate sensitivity to a doubling of CO_2 is evaluated with the 4xCO_2 experiment through the method detailed in Gregory et al. (2004). Annual mean top-of-atmosphere net downward radiative flux, F_{TOA}, is regressed on the annual mean global mean surface temperature anomaly, T_{anom}, producing slope a and intercept b:

$$F_{TOA} = aT_{anom} + b \tag{3}$$

T_{anom} is the difference between the global mean surface temperature and the time-mean global mean surface temperature from the final 100 years of the piControl simulation. The global mean surface temperature anomaly corresponding to a top-of-atmosphere net downward radiative flux of zero is considered the balanced response, or equilibrium climate sensitivity (ECS), and is calculated directly as

$$ECS = -\frac{b}{a} \tag{4}$$

We derive a power spectral density-weighted period to objectively assess the period of the QBO. A Fourier transform is applied to the daily zonal mean zonal wind averaged between 10°S and 10°N at each vertical level, and the period of the QBO, T_{QBO}, is estimated by weighting all periods by their power spectral density,

$$T_{QBO} = \frac{\sum_{n=1}^{N} P(n)/f(n)}{\sum_{n=1}^{N} P(n)} \tag{5}$$

where f is the frequency in month^{-1}, P is the power spectral density, and the sum is taken over all frequencies from $n = 1$ to N, where N is the frequency with period equal to half of the length of the time series. This summation excludes the mean, which has an infinite period.

As in Dunkerton and Delisi (1985), the QBO amplitude is estimated from the standard deviation of the climatological anomalies in the zonal mean zonal wind averaged between 10S and 10N.

Age of air is a hypothetical measure of the residence time of air within the stratosphere that captures the sum total of all transport processes (Waugh & Hall, 2002). Here we assess age of air with the artificial AOA1 tracer, which has no sinks but a linearly-increasing upward flux at the lower boundary, in contrast to (Garcia et al., 2011) which used a linearly-increasing specified lower boundary condition. For each grid point, we determine the time interval between the mixing ratio of AOA1 in a given month and the month AOA1 reached the same value at the reference latitude and pressure. We apply a 12-month running mean to AOA1 before calculating the age of air, and set the reference latitude and pressure to 0.1 °N and 100 hPa, respectively.

5 Preindustrial control climate

We begin with a brief survey of some global mean parameters in the piControl climates, displayed in Table 2, including: shortwave and longwave cloud radiative effects, global mean precipitation, global mean surface temperature, and the top-of-model net radiative imbalance. The configurations all have statistically indistinguishable top-of-model net radiative imbalances, and the shortwave and total cloud radiative effects are indistinguishable between the TSMLT and MA configurations. In all other cases, the global mean variables are statistically significantly different. In the MA 2° configuration, the shortwave and longwave cloud radiative effects are weaker, the global-mean precipitation rate is higher, and the surface temperature is warmer than in TSMLT (and MA). In the MA configuration the differences are the opposite, with stronger cloud radiative effects and a cooler surface temperature than TSMLT. Curiously, MA 2° has both the highest global mean surface temperature and highest total cloud radiative effect, which likely indicates that the cloud radiative effect is not responsible for the difference in global mean surface temperature. Overall, horizontal resolution impacts some aspects of the

Table 2. Global mean values of key variables derived from monthly mean output from the last 100 years of each piControl simulation. 95% confidence intervals assume one degree of freedom per season. Daggers indicate the value in the MA or MA 2° configuration is statistically significantly different from its value in the TSMLT configuration at the 95% confidence level, based on a two-sided t-test for the difference of means, assuming 1 degree of freedom per season.

	1 deg., TSMLT	1 deg., MA	2 deg., MA
Shortwave cloud radiative effect	-48.3±0.4 W/m^2	-48.8±0.4 W/m^2	-46.7†±0.4 W/m^2
Longwave cloud radiative effect	25.3±0.1 W/m^2	25.7†±0.1 W/m^2	22.8†±0.1 W/m^2
Total cloud radiative effect	-23.0 ±0.5 W/m^2	-23.1±0.5 W/m^2	-23.9†±0.4 W/m^2
Precipitation	2.9±0.1 mm/day	2.9†±0.1 mm/day	3.0†±0.1 mm/day
Surface temperature	287.1±0.1 K	286.9†±0.1 K	287.3†±0.1 K
Top-of-model net radiative imbalance	0.1±0.7 W/m^2	0.0±0.7 W/m^2	0.1±0.7 W/m^2

global mean climate more than the chemistry scheme. However, the differences among these configurations are generally smaller than the differences between WACCM6 and WACCM4 (Gettelman, Mills, et al., 2019).

6 Zonal mean climate and variability

A comparison of zonal mean temperatures for December-January-February and June-July-August is shown in Fig. 1. The middle and upper atmosphere exhibit a strong seasonality in temperature, with a markedly warmer stratosphere and colder mesosphere, as well as lower stratopause and mesopause, in summer (Fig. 1 a,b,f,g). MERRA2 and SABER exhibit good continuity throughout SABER's continuous-coverage latitude range (Fig. 1a,f).

The TSMLT configuration largely reflects the seasonality observed in MERRA2 & SABER (Fig. 1b,g). However, TSMLT is generally warmer in the tropics just above the stratopause and just below the mesopause (Fig. 1c,h). It's also warmer in the upper polar stratosphere in winter, and cooler in the Southern Hemisphere stratosphere in both seasons. Additionally, the summer mesosphere is slightly colder in TSMLT, such that the mesopause drops off in altitude more sharply with latitude than observed in the subtropics.

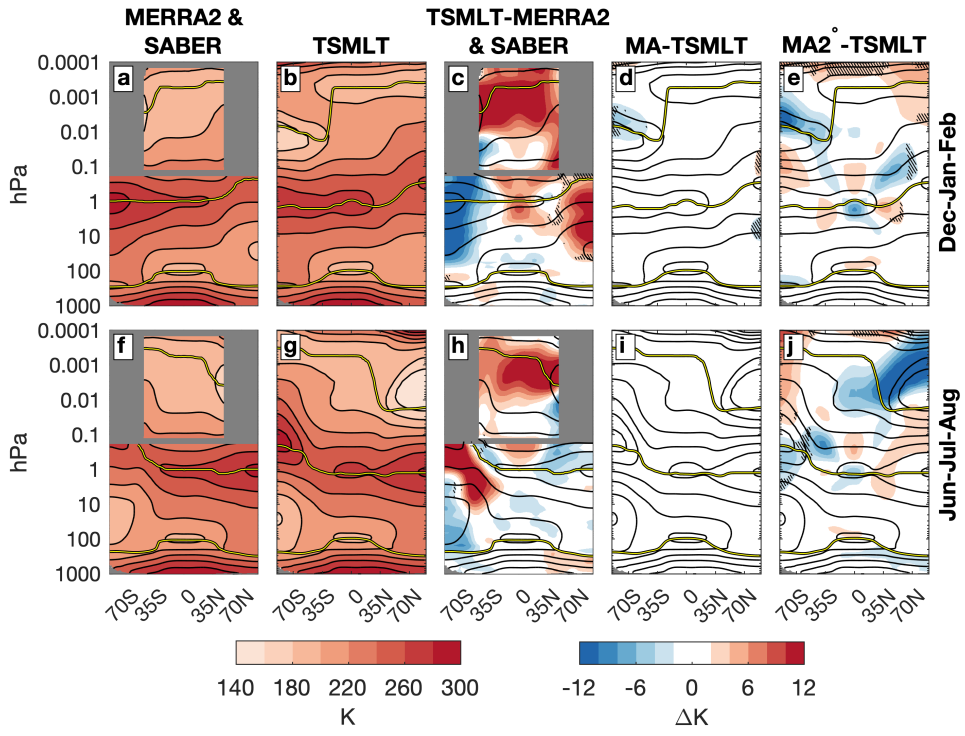

Figure 1. 1980-2015 average zonal mean temperature in (first column) MERRA2 & SABER, (second column) TSMLT, and difference in zonal mean temperature between (third column) TSMLT and MERRA2 & SABER, (fourth column) MA and TSMLT, and (fifth column) MA 2° and TSMLT, for both (top row) December-January-February and (bottom row) June-July-August. Climatology shaded in a, b, f, and g; while differences are shaded in c, d, e, h, i, and j. The MERRA2 & SABER climatology is contoured in c and h and the TSMLT climatology is contoured in d, e, i, and j. Values not statistically significantly different at the 95% confidence level are hatched. The tropopause, stratopause, and mesopause are shown by the yellow lines.

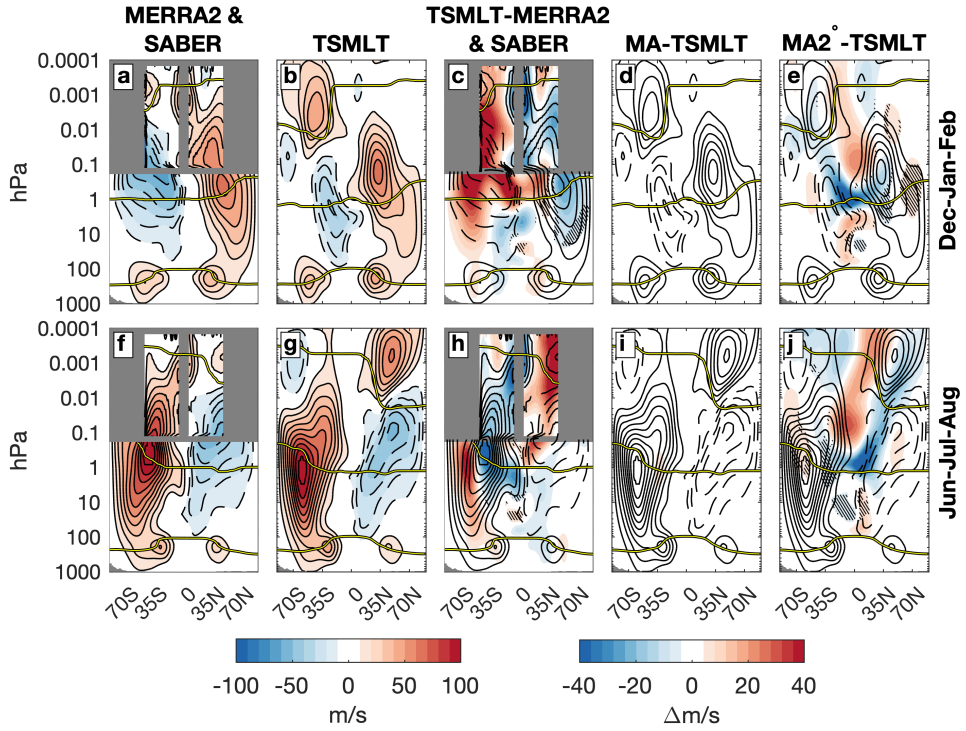

Figure 2. As in Fig. 1, but for the zonal mean zonal wind.

Simplifying the chemistry scheme has no impact on these temperature biases, even in the troposphere where the impact on chemical climate would be the largest (Fig. 1d,i). However, the zonal mean temperature in MA 2° is significantly different than in TSMLT at the summer mesopause and throughout the lower thermosphere (Fig. 1e,j). The dipole around the summer mesopause indicates the mesopause is higher in altitude in MA 2° than in TSMLT, which corrects some of the bias in TSMLT relative to SABER. On the other hand, the warmer winter and tropical lower thermosphere in MA 2° reinforces the bias already present in TSMLT relative to SABER, where SABER observations are available. Both of these differences could be related to the vertical distribution of parameterized gravity wave drag (see Fig. S1 in the Supplementary Information).

While the zonal mean surface zonal wind is set by the column-integrated momentum stress, the vertical shear in the zonal mean zonal wind at any given level is proportional to the vertically-integrated meridional temperature gradient below. In the troposphere, the symmetric equator-to-pole temperature gradient leads to westerly jets in each

hemisphere (Fig. 2a,b,f,g), which rapidly taper off into the lower stratosphere due to the reversal of the equator-to-pole temperature gradient.

On a global scale, however, the meridional temperature gradient of the stratosphere is primarily pole-to-pole. Accordingly, both the winter westerly and summer easterly stratospheric/mesospheric jet core is situated near the stratopause, where the pole-to-pole temperature gradient changes sign (Fig. 2a,b,f,g). Above the stratopause, the pole-to-pole temperature gradient maintains its sign through the mesosphere and into the lower thermosphere, leading to the winter easterly and summer westerly thermospheric jets.

In TSMLT a westerly stratospheric/mesospheric jet weaker than in MERRA2 (Fig. 2c,h) is associated with the warmer pole (Fig. 1c,h), while a westerly thermospheric jet stronger than in SABER is associated with the warmer equator. As is the case for the zonal mean temperature, there is no impact from simplifying the chemistry scheme (Fig. 2d,i). In MA 2°, minor temperature differences in the tropical mesosphere (Fig. 1e,j) are associated with significant differences in the tropical zonal mean zonal winds (Fig. 2e,j). These differences are tilted toward the summer thermosphere, where the mesopause is higher in MA 2° than in TSMLT, and tend to exacerbate the biases in the lower thermosphere (Fig. 2c,h). The differences among the model configurations are generally smaller than the model biases, however.

The climate and variability of the Northern and Southern Hemisphere stratospheric polar vortices are similarly consistent among the different configurations (Fig. 3). In both hemispheres, the vortex strength exhibits increased variability in winter due to wave forcing. From November through April, the distributions of daily Northern Hemisphere polar vortex strength in all configurations of WACCM6 are significantly different from the distributions in MERRA2 (Fig. 3a,c,e). The distributions in WACCM6 are narrower, due to both a lower maximum and higher minimum. In the Southern Hemisphere, the vortex in WACCM6 is significantly stronger throughout the seasonal cycle (Fig. 3b,d,f). Only one (major) SSW has been observed in the Southern Hemisphere over the reanalysis era, but none are simulated in WACCM6.

SSWs occur on average every two years in the Northern Hemisphere from December through March, with approximately equal frequency in all months (Fig. 4). All WACCM6 ensemble members simulate at least one November SSW, but of these, only 2 members are statistically significantly different from the frequency of 0 in MERRA2. Here, we es-

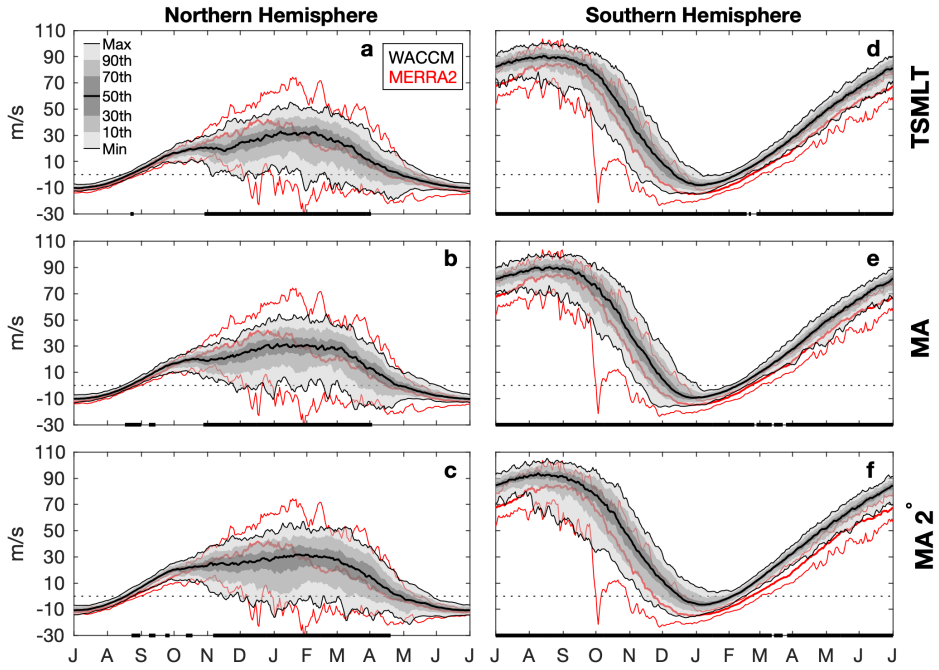

Figure 3. Stratospheric polar vortex strength for the (left column) Northern and (right column) Southern Hemisphere, in (top row) TSMLT, (middle row) MA, and (bottom row) MA 2°. WACCM6 statistics shown by black lines and shading, while the MERRA2 minimum, maximum, and median are shown by the red lines. Differences in the vortex strength distribution that are statistically significantly different at the 95% confidence level are shown by the black line along the date axis. The polar vortex is defined as the zonal mean zonal wind at 60 degrees latitude and 10 hPa.

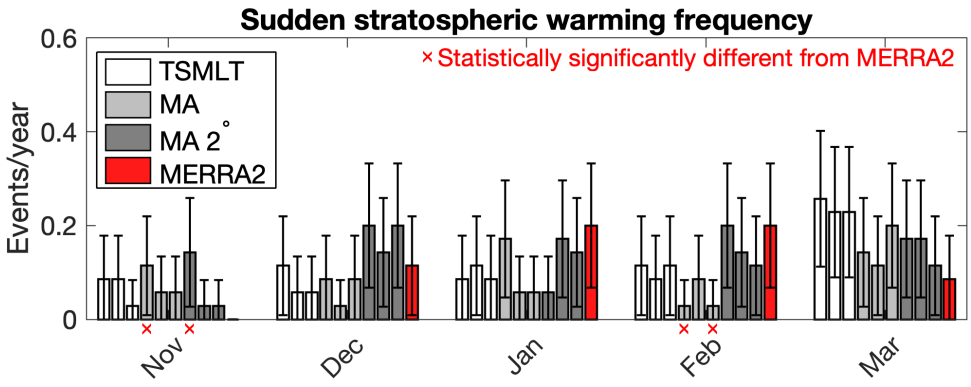

Figure 4. Northern Hemisphere sudden stratospheric warming frequency in each ensemble member and in MERRA2. 95% confidence intervals are shown as whiskers, while red x's indicate ensemble members with frequencies statistically significantly different from MERRA2 at the 95% confidence level based on a binomial distribution.

timate the monthly 95% confidence intervals using a binomial distribution based on $N = 25$ yearly samples. For a binomial distribution to be valid, we must assume that only one SSW occurs in a given month in a given year (which is never violated). These early winter SSWs in WACCM6 can be seen in the vortex statistics, where the minimum wind line becomes negative approximately one month before MERRA2 (Fig. 3a,c,e). Apart from these November SSWs, there are some MA ensemble members that simulate too few SSWs relative to MERRA2 in February. Overall, though, we do not find that the SSW frequencies in any of the WACCM6 configurations are consistently biased relative to the observed frequencies.

In the tropical stratosphere, the dominant mode of variability is the QBO (Baldwin et al., 2001), which has wide-ranging impacts on global teleconnections (Scaife et al., 2014; Toms et al., 2020). The dissipation of upward-propagating gravity, Kelvin, and mixed Rossby-gravity waves in the stratosphere drives the downward propagation of each phase of the QBO (Garcia & Richter, 2019; Holt et al., 2022), producing its characteristic 28-month period (Fig. 5a,b). In WACCM6, the spontaneously-generated QBO in TSMLT and MA has a slightly shorter period than in MERRA2 throughout the middle and upper stratosphere (Fig. 5d,e,g,h). Further, the wind anomalies are weaker than those in MERRA2 - which can be seen in the weaker QBO amplitude (Fig. 5f,i) - and they do not descend below 50 hPa (Fig. 5d,g). Instead, the tropical lower stratosphere has steady

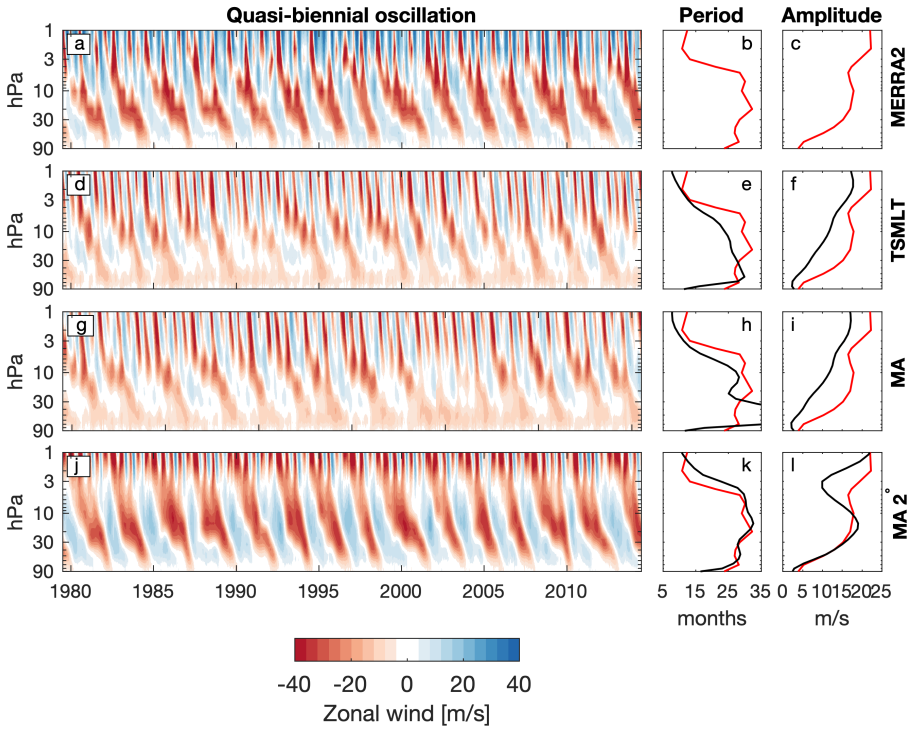

Figure 5. Daily mean zonal mean zonal wind averaged from 10°S to 10°N from (a) MERRA2 and (d,g,j) the second ensemble member of each configuration of WACCM6, (b,e,h,k) the power-weighted period of the zonal mean zonal wind, and (c,f,i,l) the QBO amplitude, with MERRA2 displayed in red.

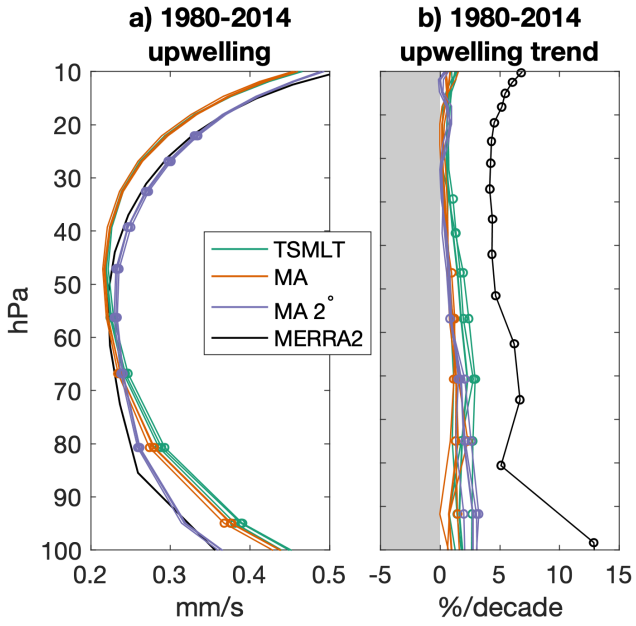

Figure 6. 1980-2014 tropical stratospheric upwelling a) mean and b) trend. Circles in a) denote values statistically significantly different from MERRA2 at the 95% confidence level, while circles in b) denote trends statistically significant at the 95% confidence level.

westerly winds. The QBO in MA 2° is highly correlated with the observed QBO in MERRA2 because it is nudged (Fig. 5j-l). However, some higher-frequency variability visible in MERRA2 (Fig. 5a) is missing in MA 2° (Fig. 5j).

Upwelling by the wave-driven residual circulation in the tropics is one the key pathways through which tracers enter the stratosphere. Both the TSMLT and MA configurations have stronger climatological stratospheric upwelling than MERRA2 below 60 hPa, whereas MA 2° has significantly stronger upwelling than MERRA2 above 80 hPa (Fig. 6a). This may be due to an apparent upward shift of the upwelling profile in the 1 degree configurations relative to both MERRA2 and the MA 2° configuration. Over the historical period, MERRA2 exhibits a statistically significant and consistent 5%/decade acceleration of upwelling at all levels. While the upwelling trends in the WACCM6 configurations are approximately 50% weaker and only significant below 30 hPa, they are consistent with one another.

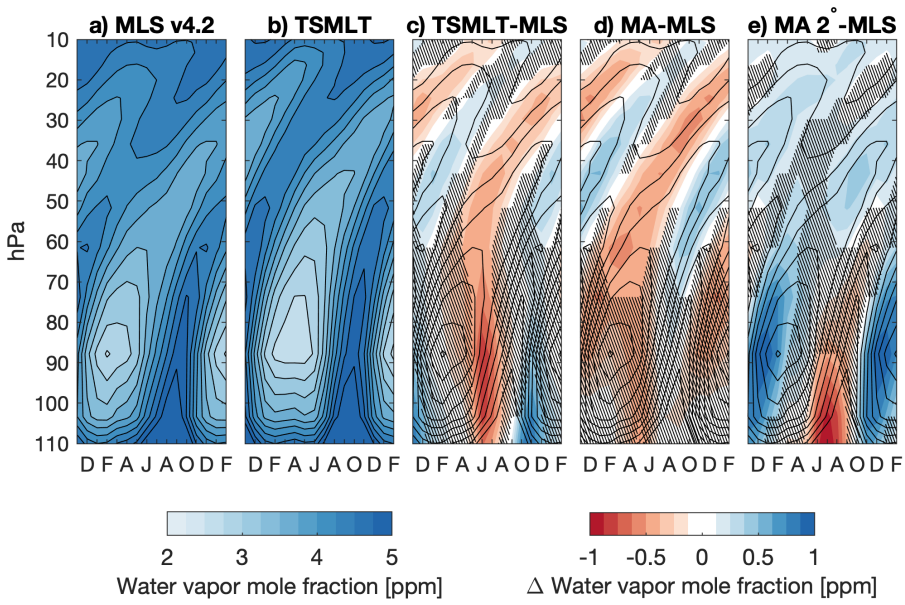

Figure 7. Tropical stratospheric water vapor averaged between 10S and 10N, with the maximum and minimum values at the model level closest to 90 hPa shown in each panel. Shading shows the climatology in a) and b), while shading shows differences in c)-e), with contours indicating the MLS climatology in c)-e). Differences not statistically significantly different from MLS at the 95% confidence level are hatched in c)-e).

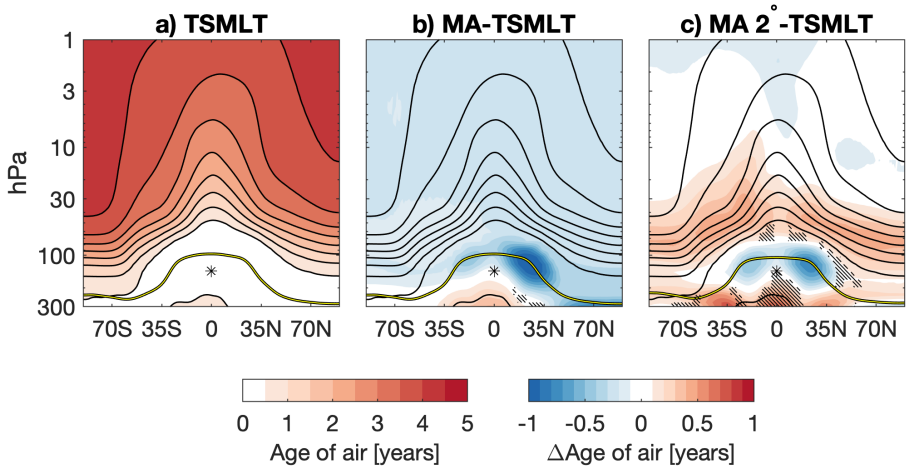

Figure 8. Stratospheric age of air averaged over the historical experiment in a) TSMLT, and b-c) the difference in age of air from TSMLT. Hatching indicates differences not statistically significant at the 95% confidence level. The tropopause is indicated by the yellow line. The reference location is indicated by the asterisk.

The residual circulation is only the advective component of the Brewer-Dobson circulation. The other component - horizontal and vertical mixing by eddies - can drive apparent vertical transport in the tropics (Glanville & Birner, 2017). The mixing ratio of water vapor at the tropical tropopause has a seasonal cycle and is quasi-conserved during ascent, excepting the source from methane oxidation, giving rise to the water vapor tape recorder (Fig. 7a,b; Mote et al. (1996)). Below 70 hPa, both the TSMLT and MA 2° configurations have a pronounced dry bias relative to MLS in boreal summer. Above 70 hPa, the 1 degree configurations are up to 0.5 ppm drier in and above the dry part of the signal, and up to 0.5 ppm wetter in and above the wet part of the signal (Fig. 7c,d). This dipole indicates stronger net ascent, with the dry signal reaching 25 hPa (Fig. 7b) rather than 30 hPa (Fig. 7a) within one year. On the other hand, MA 2° is significantly wetter than MLS throughout most of the dry part of the signal (Fig. 7e).

Age of air provides a more global perspective of stratospheric transport (Fig. 8). In the stratosphere the air is youngest at the tropopause and reaches a maximum of nearly 5 years in the polar upper stratosphere (Fig. 8a). Age of air in the MA configuration is approximately 2 months younger throughout the stratosphere, with a maximum difference of 1 year in the Northern Hemisphere subtropical jet (Fig. 8b). On the other hand,

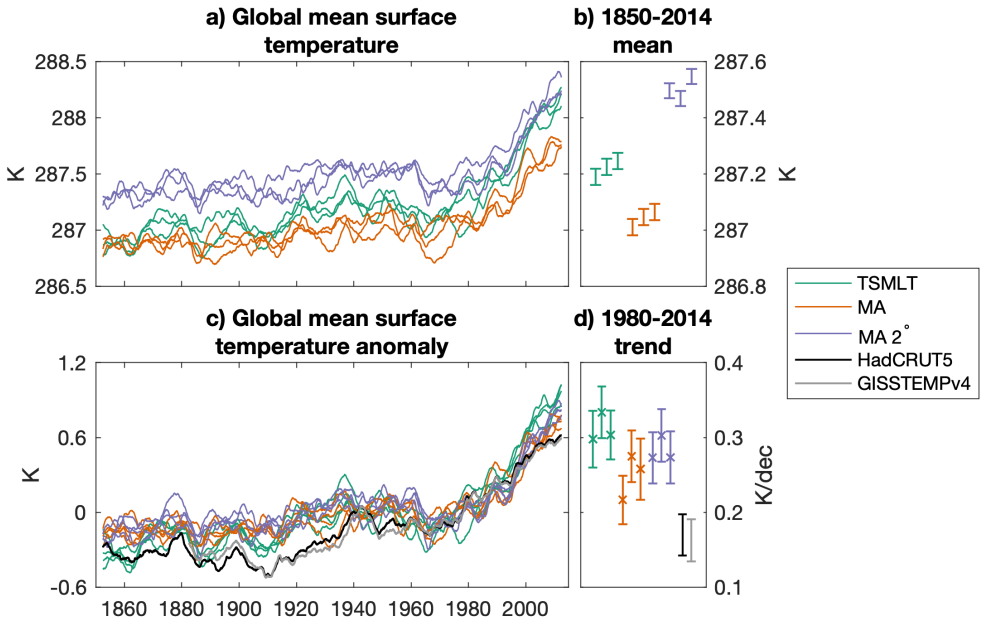

Figure 9. Time series of monthly 5-year running mean a) absolute global mean surface temperature and b) global mean surface temperature anomalies, as well as c) the 1850-2014 average global mean surface temperature and d) 1980-2014 trend in global mean surface temperature. x's in d) indicate trends statistically significantly different from both HadCRUT5 and GISSTEMPv4 at the 95% confidence level.

the age of air in the lower stratosphere in the MA 2° configuration is up to 6 months older, and oriented approximately parallel with midlatitude isentropic eddy mixing.

7 Historical climate change and climate sensitivity

An important question is whether simplified chemistry or horizontal resolution impact climate sensitivity. While the different configurations have statistically significantly different absolute global mean surface temperatures (Fig. 9a,b) - with MA cooler than TSMLT by 0.2 deg but MA 2° warmer than TSMLT by 0.3 deg, consistent with their piControl climates (Table 2) - their historical trends are similar, ranging from just over 0.2 deg/dec to 0.35 deg/dec (Fig. 9c,d). All WACCM6 ensemble members have global mean surface temperature trends statistically significantly larger than both HadCRUT5

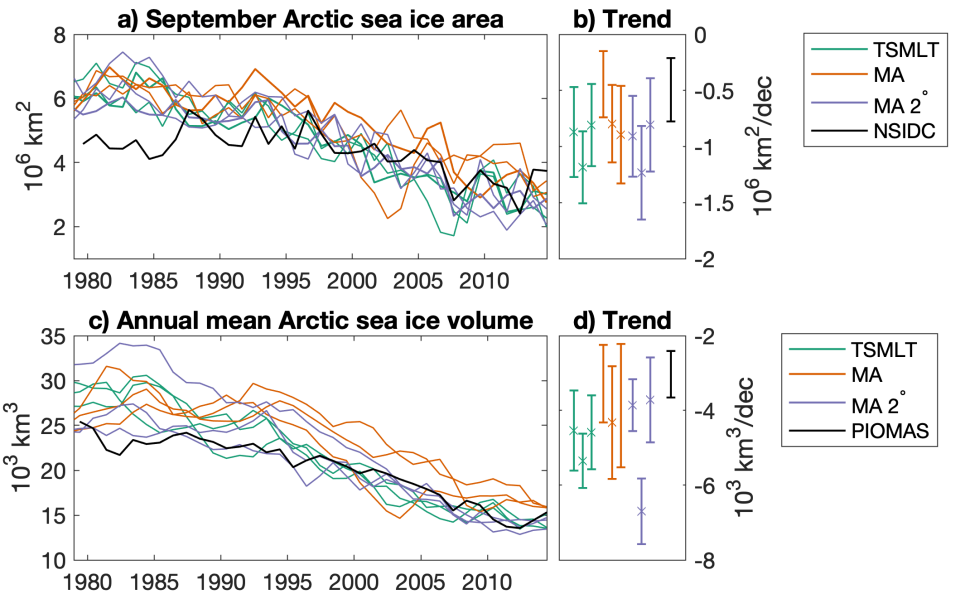

Figure 10. Time series of a) September Arctic sea ice area and b) its 1980-2014 trend, and c) Annual mean Arctic sea ice volume and d) its 1980-2014 trend. x's in b) and d) indicate trends statistically significantly different from NSIDC or PIOMAS at the 95% confidence level.

and GISSTEMPv4, which is consistent with the known higher climate sensitivity of CESM2 (Gettelman, Hannay, et al., 2019).

This enhanced response to forcings is reflected in Northern Hemisphere sea ice trends, as well (Fig. 10). September Arctic sea ice area trends are statistically significantly stronger than observed across WACCM6 configurations, with the lone exception being one MA ensemble member (Fig. 10a,b). Similarly, trends in annual mean Arctic sea ice volume are statistically significantly stronger in all TSMLT and MA 2° ensemble members than in observations (Fig. 10c,d). Only one of three MA ensemble members has an annual mean Arctic sea ice volume trend statistically significantly stronger than observed. These more negative trends are partially related to the more abundant sea ice in WACCM6 in the 1980's than was observed (Fig. 10a,c).

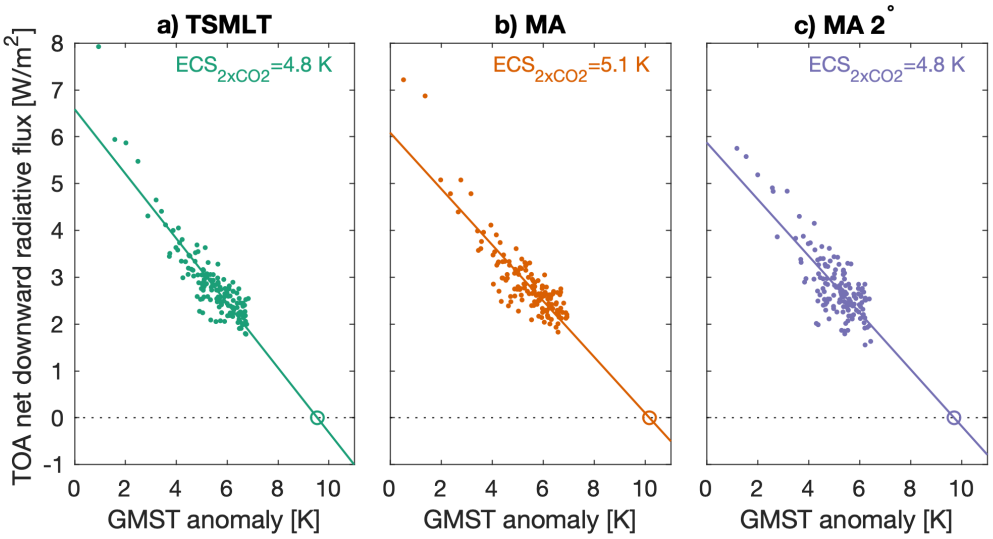

Figure 11. Equilibrium climate sensitivity estimated from the 4xCO$_2$ experiment based on the regression between the global mean surface temperature anomaly and the top-of-atmosphere net radiative flux. See text for details.

The historical simulations include a multitude of anthropogenic and natural forcings. Isolating the cause of these differences - both across ensemble members and between WACCM6 and observations - is difficult. On the other hand, the 4xCO$_2$ experiment provides a direct measure of ECS by isolating the climate response to CO$_2$ forcing alone, with the drawback that it cannot be directly constrained by observations.

All WACCM6 configurations exhibit an ECS to a doubling of CO$_2$ of around 5 K, slightly higher than the CMIP6 multi-model-mean (Zelinka et al., 2020). The cloud scheme, and in particular high latitude ice processes, are partially responsible (Gettelman, Hannay, et al., 2019). There is some nonlinearity apparent in the regression, with high top-of-atmosphere radiative flux values well above the regression line in the first few years of the experiment, and a broad cluster at higher global mean surface temperature anomalies and lower top-of-atmosphere radiative fluxes. This behavior is consistent across the different configurations, though.

In sum, we find that climate sensitivity and the simulation of historical climate variability is similar across all WACCM6 configurations and not systematically impacted by either simplified chemistry or coarser resolution.

8 Chemistry and aerosols

Here we evaluate changes in some key chemical components of the atmosphere between the model versions. In general, we don't expect the MA version to perform much differently in the stratosphere given identical chemistry schemes above the tropopause. Indeed we observe no changes in stratospheric ozone (Fig. 12a-c) except very close to the tropopause; those differences can be traced to the transport of different concentrations of ozone in tropospheric air being advected upward, as the two model configurations do show significant differences in the troposphere, particularly pronounced in the tropical upper troposphere (Fig. 12d-f). Similarities and differences between the two configurations are consistent when considering a period with no increased concentrations of halogens (1850-1900) and a period with higher halogen concentrations (2004-2010), as shown in (Fig. 12e-g) for the total tropospheric and stratospheric ozone column; the stratospheric ozone column is consistent between all model configurations except over the Antarctic, where the MA 2° configuration shows lower concentrations of around 10 DU in both periods. In the troposphere, the two MA configurations show lower ozone concentrations ranging between 4 and 2 DU; but while at higher latitudes the concentrations are more comparable, MA 2° shows lower concentrations than both 1° configurations in the tropics.

In general, the low-ozone bias of the MA 2° configuration is visible throughout the entire evolution of the Antarctic ozone hole (Fig. 13a), and is consistent with an older age of air in the polar lower stratosphere (Fig. 8c). On the other hand, the two 1° configurations present very similar evolutions up to 2100 under the SSP2-4.5 scenario. Comparisons with OMI/MLS data (Ziemke et al., 2006, 2019) for the 2004-2010 period for both the tropospheric and stratospheric ozone column in Fig. 12e-g indicates a very good agreement in the tropics, while at high Southern latitudes all model configurations seem to overestimate ozone loss (Fig. 13a). However, all of the model configurations reproduce the ozone hole anomaly relative to the 1970-1989 average (Fig. 13b). A good agreement is also present in the tropospheric column, especially, as expected, for the TSMLT configuration in the southern hemisphere and in the tropics. However, in terms of

As previous versions of CESM(WACCM) have been used extensively for the assessment of both past volcanic eruptions (Mills et al., 2016) and geoengineering (Tilmes et al., 2021), we also look at differences between the model configurations in terms of stratospheric aerosol optical depth (AOD), which is almost exclusively due to sulfates. The

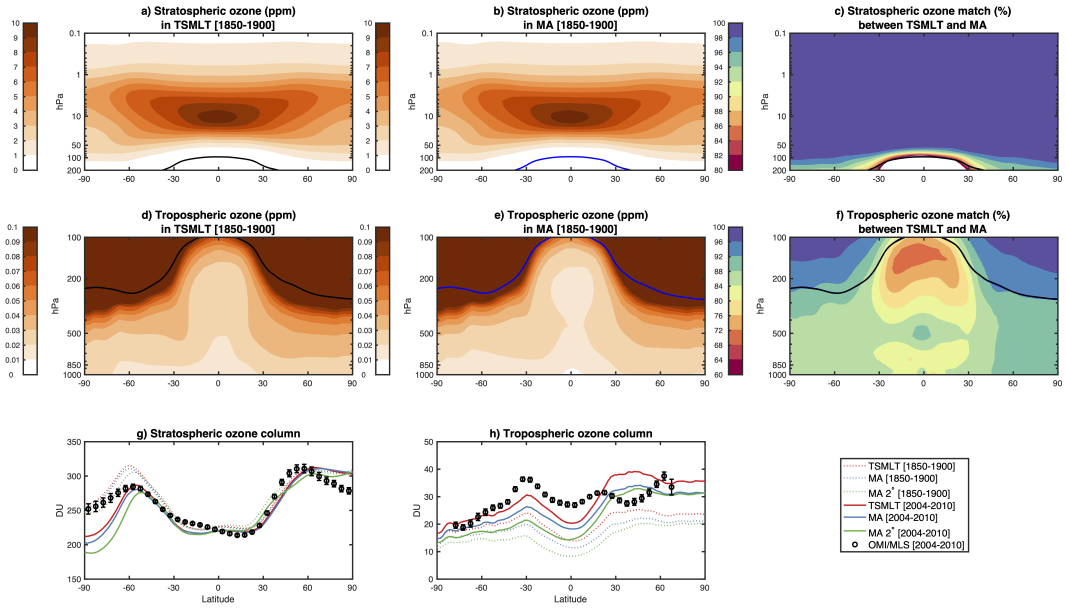

Figure 12. Comparison of atmospheric ozone between TSMLT and MA in the period 1850-1900. a-b) Stratospheric ozone concentration (ppm). c) Match (%) between the two CESM2 versions for stratospheric ozone, defined as (100 − $|O_{3,TSMLT}\text{-}O_{3,MA}|/O_{3,TSMLT}$). d-f) same as the row above, but for tropospheric ozone (note the different color scales). The tropopause pressure height averaged over the same period is also shown (black for TSMLT, blue for MA). g-h) Stratospheric and tropospheric ozone column for the two versions and for MA 2°, averaged over 1850-1900 (dashed lines) and over 2004-2010 (continuous lines), and comparison with OMI/MLS satellite data for the same period (black circles).

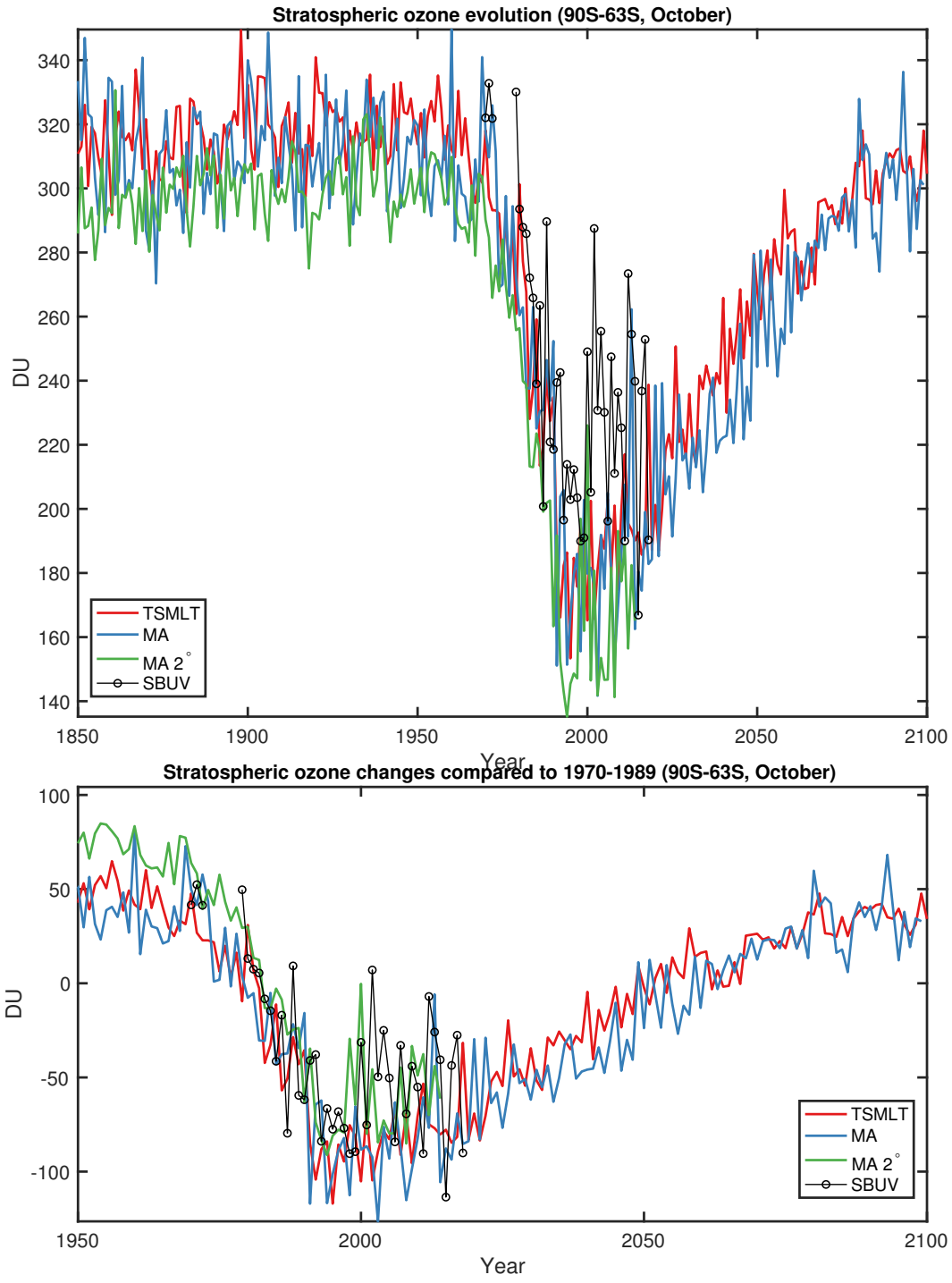

Figure 13. Evolution of Southern Hemispheric Polar Ozone column during October. Solid lines represent the ensemble averages. A comparison with the SBUV Merged Ozone Dataset is provided (black line with circles) (McPeters et al., 2013). A 3-year running mean is applied to model results. After 2015, values for the SSP2-4.5 emission scenarios are used. Values are shown for both a) absolute Dobson units and b) Dobson units relative to the 1970-1989 mean.

model configurations use the same aerosol microphysical model, MAM4 (Liu et al., 2016), but differences may arise in the concentration and evolution of aerosol precursors. Comparison is provided with the CMIP6 volcanic aerosol dataset that is available for the full 1850-2016 period (Eyring et al., 2016), with the 1980-2015 period composed of the Global Space-based Stratospheric Aerosol Climatology (GloSSAC) (Thomason et al., 2018), which combines a large series of ground and space based measurements, and the 1850-1979 period based on a 2-D interactive stratospheric aerosol model (Arfeuille et al., 2014).

Fig. 14a shows the global mean stratospheric AOD evolution in the historical period; some large differences are present in periods with no important volcanic activity (prescribed in all models from SO_2 injections following Neely III and Schmidt (2016)), where TSMLT shows a consistently lower value compared to the two MA configurations. However, in all periods with a substantive emission of SO_2 from volcanic eruptions directly in the stratosphere, the differences between the model configurations are greatly reduced, and all model configurations show similar peaks both in magnitude and in timing that coincide with the values found by GloSSAC. This change is also highlighted in Fig. 14b, where the differences with TSMLT are shown as a percentage, and the differences drop close to zero in the year following a stratospheric SO_2 injection. This indicates that differences in the baseline stratospheric aerosol load are not due to differences in the underlying stratospheric oxidation process, as also highlighted by the similarities in stratospheric OH shown in Fig. 15.

On the other hand, a comparison of tropospheric OH between the two configurations highlights large differences in MA, where the OH peak in the tropics is located lower down at 400 hPa. The background stratospheric aerosol layer, when unperturbed by the direct injection of SO_2 from volcanic sources, is largely dominated by carbonyl sulphide (COS) (Brühl et al., 2012) and surface SO_2 emissions from minor effusive volcanoes and anthropogenic sources (Neely III et al., 2013; Pitari et al., 2016); however, COS is non reactive in the troposphere and only produced SO_x after photolysis above 20 km, and its sources are independent from the model configuration. It is therefore likely that differences in the stratospheric AOD are mainly driven by differences in upper tropospheric SO_2 oxidation and subsequent transport of newly formed aerosols into the lowermost stratosphere. This is further confirmed by looking at the different aerosol modes for sulfate (Fig. S2): in quiescient periods, the main difference in the aerosol burden are found in the Aitken (smaller) mode in the upper troposphere and lower stratosphere, while in the

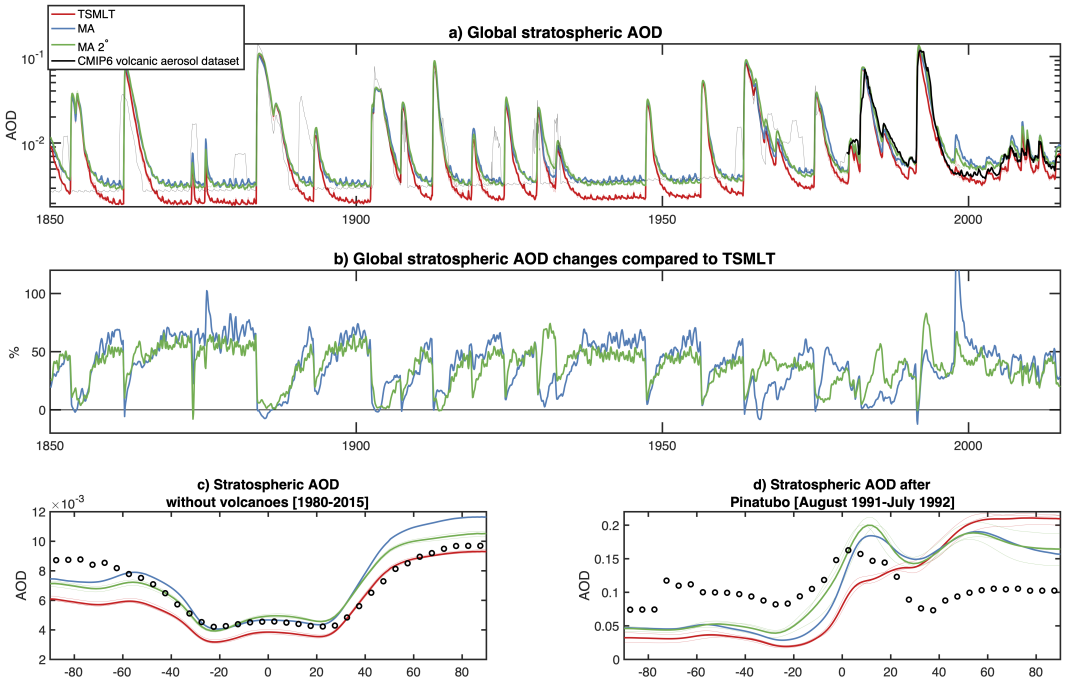

Figure 14. a) Monthly means of globally-averaged stratospheric AOD in the historical period for TSMLT (red), MA (blue), MA 2° (green) and the CMIP6 volcanic aerosol dataset (Eyring et al., 2016); the GloSSAC period (Thomason et al., 2018) [1980-2015] has been marked with a thicker line. b) percent difference between TSMLT and MA, and TSMLT and MA 2° smoothed with a 3-months running mean. c) Latitudinal mean of stratospheric AOD in periods with no volcanic activity (chosen as all months in panel a) where global stratospheric AOD does not go above 0.001) between 1980 and 2015. d) as in c), but averaged over the 18 months after the Pinatubo June 1991 eruption.

Accumulation (intermediate) and Coarse (larger) mode, the two configurations are highly comparable; and also by the larger agreement of the MA configurations with the CMIP6 volcanic aerosol dataset, which in the pre-1980 period is based solely on interactive stratospheric aerosol simulations and may thus miss the correct tropospheric contribution present in TSMLT.

The analyses of other, mostly tropospheric, aerosol species (Fig. 16) also indicate that the lack of a proper representation of oxidants due to a very simplified chemical description in the troposphere tends to not affect larger particles such as those formed by sea salt and dust, whereas black carbon and primary organic matter (POM), which are emitted in a separated, smaller primary carbon mode (Liu et al., 2016) and then aged

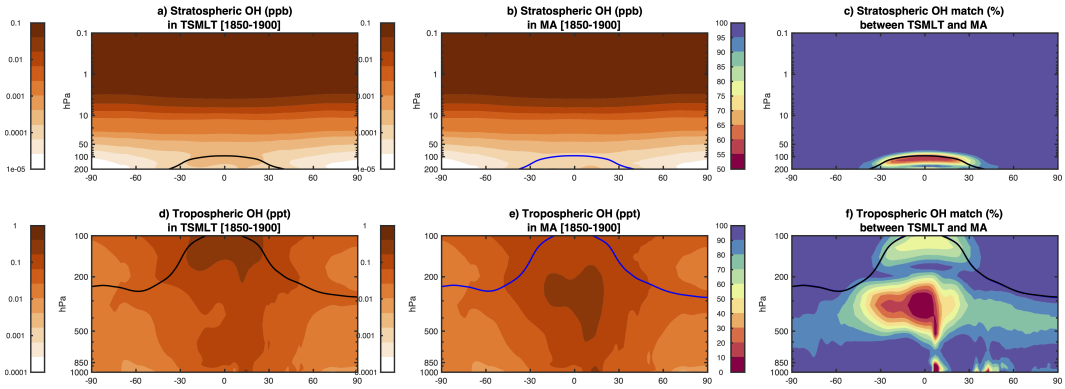

Figure 15. Comparison of atmospheric OH radical between TSMLT and MA in the historical period. a-b) Stratospheric OH concentration (ppm) between 1850 and 1900. c) Match between the two CESM2 versions for stratospheric OH defined as $(100 - |\mathrm{OH}_{TSMLT}\text{-}\mathrm{OH}_{MA}|)/\mathrm{OH}_{TSMLT})$. d-f) same as the row above, but for tropospheric OH (note the difference color scales). The tropopause pressure height averaged over the same period is also shown (black for TSMLT, blue for MA).

into larger modes, are much lower due to the lack of ageing processes into secondary organic aerosols (SOA) as present in the TMSLT configuration (Tilmes et al., 2019), which results in reduced aging of BC and POM, and therefore a slower removal. Overall, given that in MAM4 different aerosol species are treated as internally mixed for number concentration purposes (i.e., all aerosol species are described by a shared number concentration, but have different masses), this would then tend to produce similar changes in black carbon as well in the primary nucleation and Atkinson mode. Differences in surface dust as observed in Fig. 16 may on the other hand be due to slight differences in the surface climate (Fig. 9), resulting in different regional emissions.

9 Conclusions

We evaluated two simplified chemistry configurations of CESM2(WACCM6) at nominal 1 and 2 degree horizontal resolution against observations, a reanalysis, and a scientifically-validated configuration with comprehensive troposphere-stratosphere-mesosphere-lower thermosphere chemistry. Simplifying the chemistry - by eliminating halogen precursors, organic chemistry, and secondary organic aerosol formation - has little impact on zonal mean climate, middle atmosphere variability, or climate sensitivity. It does reduce the

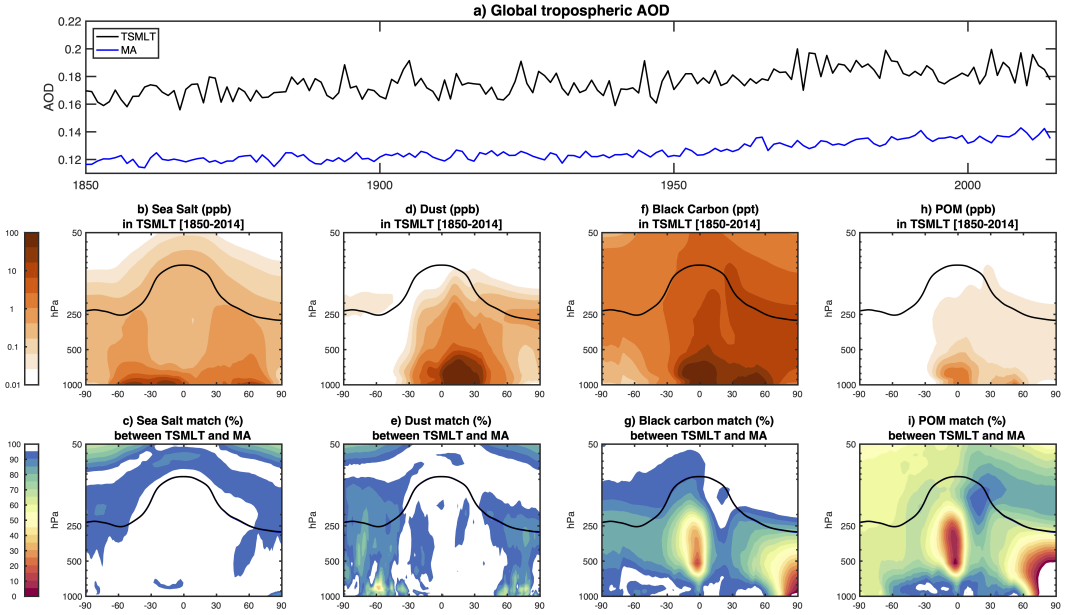

Figure 16. a) Annual means of globally-averaged tropospheric AOD in the historical period for TSMLT (black) and MA (blue). b) Sea salt concentration (ppb) in TSMLT. c) match between TSMLT and MA defined as $(100 - |\chi_{TSMLT} - \chi_{MA}|)/\chi_{TSMLT}$. d-e,f-g and h-i) same as b-c), for dust, Black carbon and POM.

absolute global mean surface temperature (of the nominal 1 degree horizontal configuration), which may be due to an elevated background stratospheric aerosol optical depth.

While there are some differences in stratospheric ozone incurred by simplifying the chemistry scheme, they are generally smaller than the impact of coarsening the nominal horizontal resolution from 1 to 2 degrees. Again, this may be due to differences in the parameterized gravity wave drag, which can be addressed with more targeted tuning in future releases. As long as model users do not require a faithful recreation of tropospheric chemistry and background aerosols in the upper troposphere/lower stratosphere, CESM2(WACCM6) with middle atmosphere chemistry can probably be used in lieu of CESM2(WACCM6) with comprehensive chemistry.

Coarsening the nominal horizontal resolution from 1 to 2 degrees has little material impact on zonal mean climate, middle atmospheric variability, or climate sensitivity, though the zonal mean circulation of the mesosphere and lower thermosphere shows some significant deviations. Where satellite observations of the upper atmosphere have adequate coverage, some of these differences tend to reduce model biases. The 2 degree

simplified chemistry configuration - without an internally-generated QBO - may be appropriate for applications where a specified QBO is acceptable.

These two configurations of CESM2(WACCM6) - nominal 1 and 2 degree horizontal resolution with middle atmosphere chemistry - are 35% and 86% computationally cheaper than the nominal 1 degree horizontal configuration of CESM2(WACCM6) with comprehensive chemistry. In some cases, they may provide support for ensemble experiments and long climate integrations to study climate change, geoengineering, and historical variability. Users will need to keep in mind the limitations of these configurations, but can be confident there are no major caveats to their zonal mean atmosphere or their global mean response to forcings. Future versions of CESM(WACCM) will continue to support economical configurations to ensure the user community has the ability to simulate the coupling of the whole atmosphere to the Sun and Earth systems.

10 Open Research

MERRA2 can be accessed from the NASA Goddard Earth Sciences (GES) Data and Information Services Center (DISC) at https://disc.gsfc.nasa.gov/datasets?project=MERRA-2 (registration may be required). SABER retrievals are accessible from GATS at http://saber.gats-inc.com/data.php, while MLS retrievals are accessible from the NASA Jet Propulsion Laboratory at https://mls.jpl.nasa.gov/ (registration may be required). The merged SBUV ozone retrievals can be downloaded directly from https://acd-ext.gsfc.nasa.gov/Data_services/merged/index.html. GISSTEMPv4 is available from the NASA Goddard Institute for Space Studies at https://data.giss.nasa.gov/gistemp/ while CRUTEM5 is available from the Met Office Hadley Centre at https://www.metoffice.gov.uk/hadobs/crutem5/. The NSIDC Sea Ice Index, Version 3, is available via FTP from https://nsidc.org/data/g02135/versions/3, and PIOMAS sea ice volume is available at http://psc.apl.uw.edu/research/projects/arctic-sea-ice-volume-anomaly/data/. All WACCM6 output is available on the Earth System Grid.

Acknowledgments

The CESM project is supported primarily by the National Science Foundation (NSF). This work was supported by the National Center for Atmospheric Research, which is a major facility sponsored by the National Science Foundation under Cooperative Agreement 1852977. Computing and data storage resources, including the Cheyenne supercomputer (doi:10.5065/D6RX99HX), were provided by the Computational and Informa-

tion Systems Laboratory (CISL) at NCAR. Portions of this study were supported by the Regional and Global Model Analysis (RGMA) component of the Earth and Environmental System Modeling Program of the U.S. Department of Energy's Office of Biological & Environmental Research (BER) via National Science Foundation IA 1844590.

References

Abalos, M., Calvo, N., Benito-Barca, S., Garny, H., Hardiman, S. C., Lin, P., ... Yoshida, K. (2021). The Brewer-Dobson circulation in CMIP6. *Atmospheric Chemistry and Physics*, *21*(17), 13571-13591. doi: 10.5194/acp-21-13571-2021

Abalos, M., Polvani, L., Calvo, N., Kinnison, D., Ploeger, F., Randel, W., & Solomon, S. (2019). New insights on the impact of ozone-depleting substances on the Brewer-Dobson circulation. *Journal of Geophysical Research: Atmospheres*, *124*(5), 2435-2451. doi: https://doi.org/10.1029/2018JD029301

Andersson, M. E., Verronen, P. T., Marsh, D. R., Päivärinta, S.-M., & Plane, J. M. C. (2016). WACCM-D: Improved modeling of nitric acid and active chlorine during energetic particle precipitation. *Journal of Geophysical Research: Atmospheres*, *121*(17), 10,328-10,341. Retrieved from `https://agupubs.onlinelibrary.wiley.com/doi/abs/10.1002/2015JD024173` doi: https://doi.org/10.1002/2015JD024173

Arfeuille, F., Weisenstein, D., Mack, H., Rozanov, E., Peter, T., & Brönnimann, S. (2014). Volcanic forcing for climate modeling: a new microphysics-based data set covering years 1600–present. *Climate of the Past*, *10*(1), 359–375.

Aubry, T. J., Staunton-Sykes, J., Marshall, L. R., Haywood, J., Abraham, N. L., & Schmidt, A. (2021). Climate change modulates the stratospheric volcanic sulfate aerosol lifecycle and radiative forcing from tropical eruptions. *Nature Communications*, *12*, 4708. doi: https://doi.org/10.1038/s41467-021-24943-7

Baldwin, M. P., Ayarzagüena, B., Birner, T., Butchart, N., Butler, A. H., Charlton-Perez, A. J., ... Pedatella, N. M. (2021). Sudden stratospheric warmings. *Reviews of Geophysics*, *59*(1), e2020RG000708. doi: https://doi.org/10.1029/2020RG000708

Baldwin, M. P., Gray, L. J., Dunkerton, T. J., Hamilton, K., Haynes, P. H., Randel, W. J., ... Takahashi, M. (2001). The quasi-biennial oscillation. *Reviews of Geophysics*, *39*(2), 179-229. Retrieved from `https://`

agupubs.onlinelibrary.wiley.com/doi/abs/10.1029/1999RG000073 doi: https://doi.org/10.1029/1999RG000073

Beljaars, A. C. M., Brown, A. R., & Wood, N. (2004). A new parametrization of turbulent orographic form drag. *Quarterly Journal of the Royal Meteorological Society*, *130*(599), 1327-1347. doi: https://doi.org/10.1256/qj.03.73

Brühl, C., Lelieveld, J., Crutzen, P. J., & Tost, H. (2012). The role of carbonyl sulphide as a source of stratospheric sulphate aerosol and its impact on climate. *Atmospheric Chemistry and Physics*, *12*(3), 1239–1253. Retrieved from https://acp.copernicus.org/articles/12/1239/2012/ doi: 10.5194/acp-12-1239-2012

Butchart, N., & Scaife, A. (2001). Removal of chlorofluorocarbons by increased mass exchange between the stratosphere and troposphere in a changing climate. *Nature*, *410*, 799-802. doi: https://doi.org/10.1038/35071047

Chabrillat, S., Kockarts, G., Fonteyn, D., & Brasseur, G. (2002). Impact of molecular diffusion on the CO2 distribution and the temperature in the mesosphere. *Geophysical Research Letters*, *29*(15), 19-1-19-4. doi: https://doi.org/10.1029/2002GL015309

Charlton, A. J., & Polvani, L. M. (2007). A new look at stratospheric sudden warmings. Part I: Climatology and modeling benchmarks. *Journal of Climate*, *20*(3), 449 - 469. Retrieved from https://journals.ametsoc.org/view/journals/clim/20/3/jcli3996.1.xml doi: 10.1175/JCLI3996.1

Chrysanthou, A., Maycock, A. C., & Chipperfield, M. P. (2020). Decomposing the response of the stratospheric Brewer-Dobson circulation to an abrupt quadrupling in CO_2. *Weather and Climate Dynamics*, *1*(1), 155–174. doi: 10.5194/wcd-1-155-2020

Damiani, A., Funke, B., López Puertas, M., Santee, M. L., Cordero, R. R., & Watanabe, S. (2016). Energetic particle precipitation: A major driver of the ozone budget in the antarctic upper stratosphere. *Geophysical Research Letters*, *43*(7), 3554-3562. doi: https://doi.org/10.1002/2016GL068279

Danabasoglu, G., Bates, S. C., Briegleb, B. P., Jayne, S. R., Jochum, M., Large, W. G., ... Yeager, S. G. (2012). The CCSM4 ocean component. *Journal of Climate*, *25*(5), 1361 - 1389. doi: 10.1175/JCLI-D-11-00091.1

Danabasoglu, G., Lamarque, J.-F., Bacmeister, J., Bailey, D. A., DuVivier, A. K.,

633 Edwards, J., ... Strand, W. G. (2020). The Community Earth System Model
634 Version 2 (CESM2). *Journal of Advances in Modeling Earth Systems*, *12*(2),
635 e2019MS001916. doi: https://doi.org/10.1029/2019MS001916

636 Dawkins, E. C. M., Feofilov, A., Rezac, L., Kutepov, A. A., Janches, D., Höffner,
637 J., ... Russell III, J. (2018). Validation of SABER v2.0 operational temper-
638 ature data with ground-based lidars in the mesosphere-lower thermosphere
639 region (75-105 km). *Journal of Geophysical Research: Atmospheres*, *123*(17),
640 9916-9934. doi: https://doi.org/10.1029/2018JD028742

641 Dunkerton, T. J., & Delisi, D. P. (1985). Climatology of the equatorial lower
642 stratosphere. *Journal of Atmospheric Sciences*, *42*(4), 376 - 396. Re-
643 trieved from `https://journals.ametsoc.org/view/journals/atsc/`
644 `42/4/1520-0469_1985_042_0376_cotels_2_0_co_2.xml` doi: 10.1175/
645 1520-0469(1985)042⟨0376:COTELS⟩2.0.CO;2

646 Emmons, L. K., Schwantes, R. H., Orlando, J. J., Tyndall, G., Kinnison, D., Lamar-
647 que, J.-F., ... Pétron, G. (2020). The chemistry mechanism in the Community
648 Earth System Model Version 2 (CESM2). *Journal of Advances in Model-*
649 *ing Earth Systems*, *12*(4), e2019MS001882. doi: https://doi.org/10.1029/
650 2019MS001882

651 Eyring, V., Bony, S., Meehl, G. A., Senior, C. A., Stevens, B., Stouffer, R. J., &
652 Taylor, K. E. (2016). Overview of the Coupled Model Intercomparison Project
653 Phase 6 (CMIP6) experimental design and organization. *Geoscientific Model*
654 *Development*, *9*(5), 1937–1958. doi: 10.5194/gmd-9-1937-2016

655 Fang, X., Pyle, J. A., Chipperfield, M. P., Daniel, J. S., Park, S., & Prinn, R. G.
656 (2019). Challenges for the recovery of the ozone layer. *Nature Geoscience*, *12*,
657 592-596. doi: https://doi.org/10.1038/s41561-019-0422-7

658 Fetterer, F., Knowles, K., Meier, W. N., Savoie, M., & Windnagel, A. K. (2017). *Sea*
659 *ice index, version 3.* Boulder, Colorado USA: NSIDC: National Snow and Ice
660 Data Center.

661 Fujiwara, M., Wright, J. S., Manney, G. L., Gray, L. J., Anstey, J., Birner, T., ...
662 Zou, C.-Z. (2017). Introduction to the SPARC Reanalysis Intercomparison
663 Project (S-RIP) and overview of the reanalysis systems. *Atmospheric Chem-*
664 *istry and Physics*, *17*(2), 1417–1452. doi: 10.5194/acp-17-1417-2017

665 Garcia, R. R., López-Puertas, M., Funke, B., Marsh, D. R., Kinnison, D. E., Smith,

A. K., & González-Galindo, F. (2014). On the distribution of CO2 and CO in the mesosphere and lower thermosphere. *Journal of Geophysical Research: Atmospheres*, *119*(9), 5700-5718. doi: https://doi.org/10.1002/2013JD021208

Garcia, R. R., Marsh, D. R., Kinnison, D. E., Boville, B. A., & Sassi, F. (2007). Simulation of secular trends in the middle atmosphere, 1950-2003. *Journal of Geophysical Research: Atmospheres*, *112*(D9). doi: https://doi.org/10.1029/2006JD007485

Garcia, R. R., Randel, W. J., & Kinnison, D. E. (2011). On the determination of age of air trends from atmospheric trace species. *Journal of the Atmospheric Sciences*, *68*(1), 139 - 154. Retrieved from `https://journals.ametsoc.org/view/journals/atsc/68/1/2010jas3527.1.xml` doi: 10.1175/2010JAS3527.1

Garcia, R. R., & Richter, J. H. (2019). On the momentum budget of the quasi-biennial oscillation in the whole atmosphere community climate model. *Journal of the Atmospheric Sciences*, *76*(1), 69 - 87. Retrieved from `https://journals.ametsoc.org/view/journals/atsc/76/1/jas-d-18-0088.1.xml` doi: 10.1175/JAS-D-18-0088.1

Garcia, R. R., Smith, A. K., Kinnison, D. E., Álvaro de la Cámara, & Murphy, D. J. (2017). Modification of the gravity wave parameterization in the Whole Atmosphere Community Climate Model: Motivation and results. *Journal of the Atmospheric Sciences*, *74*(1), 275 - 291. doi: 10.1175/JAS-D-16-0104.1

Garcia, R. R., & Solomon, S. (1985). The effect of breaking gravity waves on the dynamics and chemical composition of the mesosphere and lower thermosphere. *Journal of Geophysical Research: Atmospheres*, *90*(D2), 3850-3868. doi: https://doi.org/10.1029/JD090iD02p03850

Gelaro, R., McCarty, W., Suàrez, M. J., Todling, R., Molod, A., Takacs, L., ... Zhao, B. (2017). The Modern-Era Retrospective Analysis for Research and Applications, Version 2 (MERRA-2). *Journal of Climate*, *30*(14), 5419 - 5454. doi: 10.1175/JCLI-D-16-0758.1

Gettelman, A., Hannay, C., Bacmeister, J. T., Neale, R. B., Pendergrass, A. G., Danabasoglu, G., ... Mills, M. J. (2019). High climate sensitivity in the community earth system model version 2 (cesm2). *Geophysical Research Letters*, *46*(14), 8329-8337. Retrieved from `https://agupubs.onlinelibrary`

.wiley.com/doi/abs/10.1029/2019GL083978 doi: https://doi.org/10.1029/2019GL083978

Gettelman, A., Mills, M. J., Kinnison, D. E., Garcia, R. R., Smith, A. K., Marsh, D. R., ... Randel, W. J. (2019). The Whole Atmosphere Community Climate Model Version 6 (WACCM6). *Journal of Geophysical Research: Atmospheres*, *124*(23), 12380-12403. doi: https://doi.org/10.1029/2019JD030943

Gettelman, A., & Morrison, H. (2015). Advanced two-moment bulk microphysics for global models. Part I: Off-line tests and comparison with other schemes. *Journal of Climate*, *28*(3), 1268 - 1287. doi: 10.1175/JCLI-D-14-00102.1

Glanville, A. A., & Birner, T. (2017). Role of vertical and horizontal mixing in the tape recorder signal near the tropical tropopause. *Atmospheric Chemistry and Physics*, *17*(6), 4337–4353. doi: 10.5194/acp-17-4337-2017

Global Modeling and Assimilation Office (GMAO). (2015). *inst3_3d_asm_Np: MERRA-2 3D IAU State, Meteorology Instantaneous 3-hourly (p-coord, 0.625x0.5L42), version 5.12.4.* https://www.nasa.gov/nh/pluto-the-other-red-planet. Greenbelt, MD, USA: Goddard Space Flight Center Distributed Active Archive Center (GSFC DAAC). doi: 10.5067/QBZ6MG944HW0

Golaz, J.-C., Larson, V. E., & Cotton, W. R. (2002). A PDF-Based Model for Boundary Layer Clouds. Part I: Method and Model Description. *Journal of the Atmospheric Sciences*, *59*(24), 3540 - 3551. doi: 10.1175/1520-0469(2002)059⟨3540:APBMFB⟩2.0.CO;2

Gregory, J. M., Ingram, W. J., Palmer, M. A., Jones, G. S., Stott, P. A., Thorpe, R. B., ... Williams, K. D. (2004). A new method for diagnosing radiative forcing and climate sensitivity. *Geophysical Research Letters*, *31*(3). doi: https://doi.org/10.1029/2003GL018747

Hodzic, A., Kasibhatla, P. S., Jo, D. S., Cappa, C. D., Jimenez, J. L., Madronich, S., & Park, R. J. (2016). Rethinking the global secondary organic aerosol (SOA) budget: stronger production, faster removal, shorter lifetime. *Atmospheric Chemistry and Physics*, *16*(12), 7917–7941. doi: 10.5194/acp-16-7917-2016

Holt, L. A., Lott, F., Garcia, R. R., Kiladis, G. N., Cheng, Y.-M., Anstey, J. A., ... Yukimoto, S. (2022). An evaluation of tropical waves and

wave forcing of the QBO in the QBOi models. *Quarterly Journal of the Royal Meteorological Society*, *148*(744), 1541-1567. Retrieved from https://rmets.onlinelibrary.wiley.com/doi/abs/10.1002/qj.3827 doi: https://doi.org/10.1002/qj.3827

Hunke, E. C., Lipscomb, W. H., Turner, A. K., Jeffery, N., & Elliott, S. (2015). *CICE: The Los Alamos Sea Ice Model. Documentation and Software User's Manual. Version 5.1.* Los Alamos National Laboratory, Tech. Rep. LA-CC-06-012: T-3 Fluid Dynamics Group.

Iacono, M. J., Delamere, J. S., Mlawer, E. J., Shephard, M. W., Clough, S. A., & Collins, W. D. (2008). Radiative forcing by long-lived greenhouse gases: Calculations with the AER radiative transfer models. *Journal of Geophysical Research: Atmospheres*, *113*(D13). doi: https://doi.org/10.1029/2008JD009944

Kinnison, D. E., Brasseur, G. P., Walters, S., Garcia, R. R., Marsh, D. R., Sassi, F., ... Simmons, A. J. (2007). Sensitivity of chemical tracers to meteorological parameters in the MOZART-3 chemical transport model. *Journal of Geophysical Research: Atmospheres*, *112*(D20). doi: https://doi.org/10.1029/2006JD007879

Kravitz, B., Robock, A., Tilmes, S., Boucher, O., English, J. M., Irvine, P. J., ... Watanabe, S. (2015). The Geoengineering Model Intercomparison Project Phase 6 (GeoMIP6): Simulation design and preliminary results. *Geoscientific Model Development*, *8*(10), 3379–3392. doi: 10.5194/gmd-8-3379-2015

Lambert, A., Read, W. G., Livesey, N. J., Santee, M. L., Manney, G. L., Froidevaux, L., ... Atlas, E. (2007). Validation of the Aura Microwave Limb Sounder middle atmosphere water vapor and nitrous oxide measurements. *Journal of Geophysical Research: Atmospheres*, *112*(D24). doi: https://doi.org/10.1029/2007JD008724

Larson, V. E. (2017). CLUBB-SILHS: A parameterization of subgrid variability in the atmosphere. *arXiv preprint arXiv:1711.03675*.

Lawrence, D. M., Fisher, R. A., Koven, C. D., Oleson, K. W., Swenson, S. C., Bonan, G., ... Zeng, X. (2019). The Community Land Model Version 5: Description of new features, benchmarking, and impact of forcing uncertainty. *Journal of Advances in Modeling Earth Systems*, *11*(12), 4245-4287. doi: https://doi.org/10.1029/2018MS001583

765 Lenssen, N. J. L., Schmidt, G. A., Hansen, J. E., Menne, M. J., Persin, A., Ruedy,
766 R., & Zyss, D. (2019). Improvements in the gistemp uncertainty model.
767 *Journal of Geophysical Research: Atmospheres*, *124*(12), 6307-6326. doi:
768 https://doi.org/10.1029/2018JD029522

769 Li, H., Wigmosta, M. S., Wu, H., Huang, M., Ke, Y., Coleman, A. M., & Leung,
770 L. R. (2013). A physically based runoff routing model for land surface and
771 earth system models. *Journal of Hydrometeorology*, *14*(3), 808 - 828. doi:
772 10.1175/JHM-D-12-015.1

773 Lin, S.-J., & Rood, R. B. (1997). An explicit flux-form semi-lagrangian shallow-
774 water model on the sphere. *Quarterly Journal of the Royal Meteorological Soci-*
775 *ety*, *123*(544), 2477-2498. doi: https://doi.org/10.1002/qj.49712354416

776 Liu, X., Ma, P.-L., Wang, H., Tilmes, S., Singh, B., Easter, R. C., ... Rasch,
777 P. J. (2016). Description and evaluation of a new four-mode version of the
778 Modal Aerosol Module (MAM4) within version 5.3 of the Community At-
779 mosphere Model. *Geoscientific Model Development*, *9*(2), 505–522. doi:
780 10.5194/gmd-9-505-2016

781 Maliniemi, V., Nesse Tyssøy, H., Smith-Johnsen, C., Arsenovic, P., & Marsh,
782 D. R. (2021). Effects of enhanced downwelling of no_x on antarctic upper-
783 stratospheric ozone in the 21st century. *Atmospheric Chemistry and Physics*,
784 *21*(14), 11041–11052. Retrieved from `https://acp.copernicus.org/`
785 `articles/21/11041/2021/` doi: 10.5194/acp-21-11041-2021

786 McPeters, R. D., Bhartia, P. K., Haffner, D., Labow, G. J., & Flynn, L. (2013). The
787 version 8.6 sbuv ozone data record: An overview. *Journal of Geophysical Re-*
788 *search: Atmospheres*, *118*(14), 8032-8039. Retrieved from `https://agupubs`
789 `.onlinelibrary.wiley.com/doi/abs/10.1002/jgrd.50597` doi: https://doi
790 .org/10.1002/jgrd.50597

791 Meraner, K., & Schmidt, H. (2018). Climate impact of idealized winter polar
792 mesospheric and stratospheric ozone losses as caused by energetic particle
793 precipitation. *Atmospheric Chemistry and Physics*, *18*(2), 1079–1089. doi:
794 10.5194/acp-18-1079-2018

795 Mills, M. J., Richter, J. H., Tilmes, S., Kravitz, B., MacMartin, D. G., Glanville,
796 A. A., ... Kinnison, D. E. (2017). Radiative and chemical response to inter-
797 active stratospheric sulfate aerosols in fully coupled cesm1(waccm). *Jour-*

nal of Geophysical Research: Atmospheres, *122*(23), 13,061-13,078. doi: https://doi.org/10.1002/2017JD027006

Mills, M. J., Schmidt, A., Easter, R., Solomon, S., Kinnison, D. E., Ghan, S. J., ... Gettelman, A. (2016). Global volcanic aerosol properties derived from emissions, 1990-2014, using CESM1(WACCM). *Journal of Geophysical Research: Atmospheres*, *121*(5), 2332-2348. doi: https://doi.org/10.1002/2015JD024290

Mlawer, E. J., Taubman, S. J., Brown, P. D., Iacono, M. J., & Clough, S. A. (1997). Radiative transfer for inhomogeneous atmospheres: RRTM, a validated correlated-k model for the longwave. *Journal of Geophysical Research: Atmospheres*, *102*(D14), 16663-16682. doi: https://doi.org/10.1029/97JD00237

Molod, A., Takacs, L., Suarez, M., & Bacmeister, J. (2015). Development of the GEOS-5 atmospheric general circulation model: evolution from MERRA to MERRA2. *Geoscientific Model Development*, *8*(5), 1339–1356. doi: 10.5194/gmd-8-1339-2015

Morice, C. P., Kennedy, J. J., Rayner, N. A., & Jones, P. D. (2012). Quantifying uncertainties in global and regional temperature change using an ensemble of observational estimates: The hadcrut4 data set. *Journal of Geophysical Research: Atmospheres*, *117*(D8). doi: https://doi.org/10.1029/2011JD017187

Mote, P. W., Rosenlof, K. H., McIntyre, M. E., Carr, E. S., Gille, J. C., Holton, J. R., ... Waters, J. W. (1996). An atmospheric tape recorder: The imprint of tropical tropopause temperatures on stratospheric water vapor. *Journal of Geophysical Research: Atmospheres*, *101*(D2), 3989-4006. doi: https://doi.org/10.1029/95JD03422

National Academies of Sciences, Engineering, and Medicine. (2021). *Reflecting sunlight: Recommendations for solar geoengineering research and research governance*. Washington, D. C.: The National Academies Press. doi: https://doi.org/10.17226/25762

Neely III, R. R., & Schmidt, A. (2016). Volcaneesm: Global volcanic sulphur dioxide (SO2) emissions database from 1850 to present.

Neely III, R. R., Toon, O. B., Solomon, S., Vernier, J.-P., Alvarez, C., English, J. M., ... Thayer, J. P. (2013). Recent anthropogenic increases in so2 from asia have minimal impact on stratospheric aerosol. *Geophysical Research Letters*, *40*(5), 999-1004. Retrieved from `https://`

agupubs.onlinelibrary.wiley.com/doi/abs/10.1002/grl.50263 doi: https://doi.org/10.1002/grl.50263

Neu, J. L., Flury, T., Manney, G. L., Santee, M. L., Livesey, N. J., & Worden, J. (2014). Tropospheric ozone variations governed by changes in stratospheric circulation. *Nature Geoscience*, *7*(5), 340-344. doi: https://doi.org/10.1038/ngeo2138

Pedatella, N. M., Richter, J. H., Edwards, J., & Glanville, A. A. (2021). Predictability of the mesosphere and lower thermosphere during major sudden stratospheric warmings. *Geophysical Research Letters*, *48*(15), e2021GL093716. Retrieved from https://agupubs.onlinelibrary.wiley.com/doi/abs/10.1029/2021GL093716 (e2021GL093716 2021GL093716) doi: https://doi.org/10.1029/2021GL093716

Pitari, G., Visioni, D., Mancini, E., Cionni, I., Di Genova, G., & Gandolfi, I. (2016). Sulfate aerosols from non-explosive volcanoes: Chemical-radiative effects in the troposphere and lower stratosphere. *Atmosphere*, *7*(7). Retrieved from https://www.mdpi.com/2073-4433/7/7/85 doi: 10.3390/atmos7070085

Plane, J. M. C. (2012). Cosmic dust in the earth's atmosphere. *Chemical Society Reviews*, *41*, 6507-6518. doi: 10.1039/C2CS35132C

Polvani, L. M., Wang, L., Abalos, M., Butchart, N., Chipperfield, M. P., Dameris, M., ... Stone, K. A. (2019). Large impacts, past and future, of ozone-depleting substances on Brewer-Dobson circulation trends: A multimodel assessment. *Journal of Geophysical Research: Atmospheres*, *124*(13), 6669-6680. doi: https://doi.org/10.1029/2018JD029516

Randel, W. J., Smith, A. K., Wu, F., Zou, C.-Z., & Qian, H. (2016). Stratospheric temperature trends over 1979-2015 derived from combined SSU, MLS, and SABER satellite observations. *Journal of Climate*, *29*(13), 4843 - 4859. doi: 10.1175/JCLI-D-15-0629.1

Remsberg, E. E., Marshall, B. T., Garcia-Comas, M., Krueger, D., Lingenfelser, G. S., Martin-Torres, J., ... Thompson, R. E. (2008). Assessment of the quality of the Version 1.07 temperature-versus-pressure profiles of the middle atmosphere from TIMED/SABER. *Journal of Geophysical Research: Atmospheres*, *113*(D17). doi: https://doi.org/10.1029/2008JD010013

Richter, J. H., Sassi, F., & Garcia, R. R. (2010). Toward a physically based gravity

wave source parameterization in a general circulation model. *Journal of the Atmospheric Sciences*, *67*(1), 136 - 156. doi: 10.1175/2009JAS3112.1

Rugenstein, M., Bloch-Johnson, J., Gregory, J., Andrews, T., Mauritsen, T., Li, C., ... Knutti, R. (2020). Equilibrium climate sensitivity estimated by equilibrating climate models. *Geophysical Research Letters*, *47*(4), e2019GL083898. doi: https://doi.org/10.1029/2019GL083898

Scaife, A. A., Athanassiadou, M., Andrews, M., Arribas, A., Baldwin, M., Dunstone, N., ... Williams, A. (2014). Predictability of the quasi-biennial oscillation and its northern winter teleconnection on seasonal to decadal timescales. *Geophysical Research Letters*, *41*(5), 1752-1758. Retrieved from `https://agupubs.onlinelibrary.wiley.com/doi/abs/10.1002/2013GL059160` doi: https://doi.org/10.1002/2013GL059160

Schweiger, A., Lindsay, R., Zhang, J., Steele, M., Stern, H., & Kwok, R. (2011). Uncertainty in modeled arctic sea ice volume. *Journal of Geophysical Research: Oceans*, *116*(C8). doi: https://doi.org/10.1029/2011JC007084

Scinocca, J. F., & McFarlane, N. A. (2000). The parametrization of drag induced by stratified flow over anisotropic orography. *Quarterly Journal of the Royal Meteorological Society*, *126*(568), 2353-2393. doi: https://doi.org/10.1002/qj.49712656802

Sinnhuber, M., Berger, U., Funke, B., Nieder, H., Reddmann, T., Stiller, G., ... Wissing, J. M. (2018). NO_y production, ozone loss and changes in net radiative heating due to energetic particle precipitation in 2002-2010. *Atmospheric Chemistry and Physics*, *18*(2), 1115–1147. doi: 10.5194/acp-18-1115-2018

Sinnhuber, M., Nieder, H., & Wieters, N. (2012). Energetic particle precipitation and the chemistry of the mesosphere/lower thermosphere. *Surveys in Geophysics*, *33*(6), 1281-1334. doi: 10.1007/s10712-012-9201-3

Smith, A. K., Garcia, R. R., Marsh, D. R., & Richter, J. H. (2011). WACCM simulations of the mean circulation and trace species transport in the winter mesosphere. *Journal of Geophysical Research: Atmospheres*, *116*(D20). doi: https://doi.org/10.1029/2011JD016083

Solomon, S. (1999). Stratospheric ozone depletion: A review of concepts and history. *Reviews of Geophysics*, *37*(3), 275-316. doi: https://doi.org/10.1029/1999RG900008

Solomon, S., Dube, K., Stone, K., Yu, P., Kinnison, D., Toon, O. B., ... Degenstein, D. (2022). On the stratospheric chemistry of midlatitude wildfire smoke. *Proceedings of the National Academy of Sciences*, *119*(10), e2117325119. doi: 10.1073/pnas.2117325119

Solomon, S., Garcia, R., Rowland, F. S., & Wuebbles, D. J. (1986). On the depletion of antarctic ozone. *Nature*, *321*, 755–758. doi: https://doi.org/10.1038/321755a0

Thomason, L. W., Ernest, N., Millán, L., Rieger, L., Bourassa, A., Vernier, J.-P., ... Peter, T. (2018). A global space-based stratospheric aerosol climatology: 1979–2016. *Earth System Science Data*, *10*(1), 469–492.

Tilmes, S., Hodzic, A., Emmons, L. K., Mills, M. J., Gettelman, A., Kinnison, D. E., ... Liu, X. (2019). Climate forcing and trends of organic aerosols in the Community Earth System Model (CESM2). *Journal of Advances in Modeling Earth Systems*, *11*(12), 4323-4351. doi: https://doi.org/10.1029/2019MS001827

Tilmes, S., MacMartin, D. G., Lenaerts, J. T. M., van Kampenhout, L., Muntjewerf, L., Xia, L., ... Robock, A. (2020). Reaching 1.5 and 2.0 ° global surface temperature targets using stratospheric aerosol geoengineering. *Earth System Dynamics*, *11*(3), 579–601. doi: 10.5194/esd-11-579-2020

Tilmes, S., Richter, J. H., Kravitz, B., MacMartin, D. G., Glanville, A. S., Visioni, D., ... Müller, R. (2021). Sensitivity of total column ozone to stratospheric sulfur injection strategies. *Geophysical Research Letters*, *48*(19), e2021GL094058. doi: https://doi.org/10.1029/2021GL094058

Tilmes, S., Visioni, D., Jones, A., Haywood, J., Séférian, R., Nabat, P., ... Niemeier, U. (2022). Stratospheric ozone response to sulfate aerosol and solar dimming climate interventions based on the G6 Geoengineering Model Intercomparison Project (GeoMIP) simulations. *Atmospheric Chemistry and Physics*, *22*(7), 4557–4579. doi: 10.5194/acp-22-4557-2022

Toms, B. A., Barnes, E. A., Maloney, E. D., & van den Heever, S. C. (2020). The global teleconnection signature of the madden-julian oscillation and its modulation by the quasi-biennial oscillation. *Journal of Geophysical Research: Atmospheres*, *125*(7), e2020JD032653. Retrieved from `https://agupubs.onlinelibrary.wiley.com/doi/abs/10.1029/2020JD032653` (e2020JD032653 10.1029/2020JD032653) doi: https://doi.org/10.1029/

2020JD032653

Verronen, P. T., Andersson, M. E., Marsh, D. R., Kovács, T., & Plane, J. M. C. (2016). WACCM-D: Whole Atmosphere Community Climate Model with D-region ion chemistry. *Journal of Advances in Modeling Earth Systems*, *8*(2), 954-975. Retrieved from `https://agupubs.onlinelibrary.wiley.com/doi/abs/10.1002/2015MS000592` doi: https://doi.org/10.1002/2015MS000592

Visioni, D., MacMartin, D. G., Kravitz, B., Boucher, O., Jones, A., Lurton, T., ... Tilmes, S. (2021). Identifying the sources of uncertainty in climate model simulations of solar radiation modification with the G6sulfur and G6solar Geoengineering Model Intercomparison Project (GeoMIP) simulations. *Atmospheric Chemistry and Physics*, *21*(13), 10039–10063. doi: 10.5194/acp-21-10039-2021

Visioni, D., MacMartin, D. G., Kravitz, B., Lee, W., Simpson, I. R., & Richter, J. H. (2020). Reduced poleward transport due to stratospheric heating under stratospheric aerosols geoengineering. *Geophysical Research Letters*, *47*(17), e2020GL089470. doi: https://doi.org/10.1029/2020GL089470

Visioni, D., Tilmes, S., Bardeen, C., Mills, M., MacMartin, D. G., Kravitz, B., & Richter, J. H. (2022). Limitations of assuming internal mixing between different aerosol species: a case study with sulfate geoengineering simulations. *Atmospheric Chemistry and Physics*, *22*(3), 1739–1756. doi: 10.5194/acp-22-1739-2022

Waugh, D., & Hall, T. (2002). Age of stratospheric air: Theory, observations, and models. *Reviews of Geophysics*, *40*(4), 1-1-1-26. Retrieved from `https://agupubs.onlinelibrary.wiley.com/doi/abs/10.1029/2000RG000101` doi: https://doi.org/10.1029/2000RG000101

Weisenstein, D. K., Visioni, D., Franke, H., Niemeier, U., Vattioni, S., Chiodo, G., ... Keith, D. W. (2022). An interactive stratospheric aerosol model intercomparison of solar geoengineering by stratospheric injection of SO_2 or accumulation-mode sulfuric acid aerosols. *Atmospheric Chemistry and Physics*, *22*(5), 2955–2973. doi: 10.5194/acp-22-2955-2022

Zelinka, M. D., Myers, T. A., McCoy, D. T., Po-Chedley, S., Caldwell, P. M., Ceppi, P., ... Taylor, K. E. (2020). Causes of higher climate sensitivity in cmip6 models. *Geophysical Research Letters*, *47*(1), e2019GL085782. doi:

https://doi.org/10.1029/2019GL085782

Zhang, G. J., & McFarlane, N. M. (1995). Sensitivity of climate simulations to the parameterization of cumulus convection in the canadian climate centre general circulation model. *Atmosphere-Ocean*, *33*(3), 407-446. doi: 10.1080/07055900.1995.9649539

Zhang, J., & Rothrock, D. A. (2003). Modeling global sea ice with a thickness and enthalpy distribution model in generalized curvilinear coordinates. *Monthly Weather Review*, *131*(5), 845 - 861. Retrieved from `https://journals.ametsoc.org/view/journals/mwre/131/5/1520-0493_2003_131_0845_mgsiwa_2.0.co_2.xml` doi: 10.1175/1520-0493(2003)131⟨0845:MGSIWA⟩2.0.CO;2

Zhang, J., Wuebbles, D., Kinnison, D., & Baughcum, S. L. (2021). Stratospheric ozone and climate forcing sensitivity to cruise altitudes for fleets of potential supersonic transport aircraft. *Journal of Geophysical Research: Atmospheres*, *126*(16), e2021JD034971. doi: https://doi.org/10.1029/2021JD034971

Ziemke, J. R., Chandra, S., Duncan, B. N., Froidevaux, L., Bhartia, P. K., Levelt, P. F., & Waters, J. W. (2006). Tropospheric ozone determined from Aura OMI and MLS: Evaluation of measurements and comparison with the Global Modeling Initiative's Chemical Transport Model. *Journal of Geophysical Research: Atmospheres*, *111*(D19). Retrieved from `https://agupubs.onlinelibrary.wiley.com/doi/abs/10.1029/2006JD007089` doi: https://doi.org/10.1029/2006JD007089

Ziemke, J. R., Oman, L. D., Strode, S. A., Douglass, A. R., Olsen, M. A., McPeters, R. D., ... Taylor, S. L. (2019). Trends in global tropospheric ozone inferred from a composite record of TOMS/OMI/MLS/OMPS satellite measurements and the MERRA-2 GMI simulation. *Atmospheric Chemistry and Physics*, *19*(5), 3257–3269.

Figure 1.

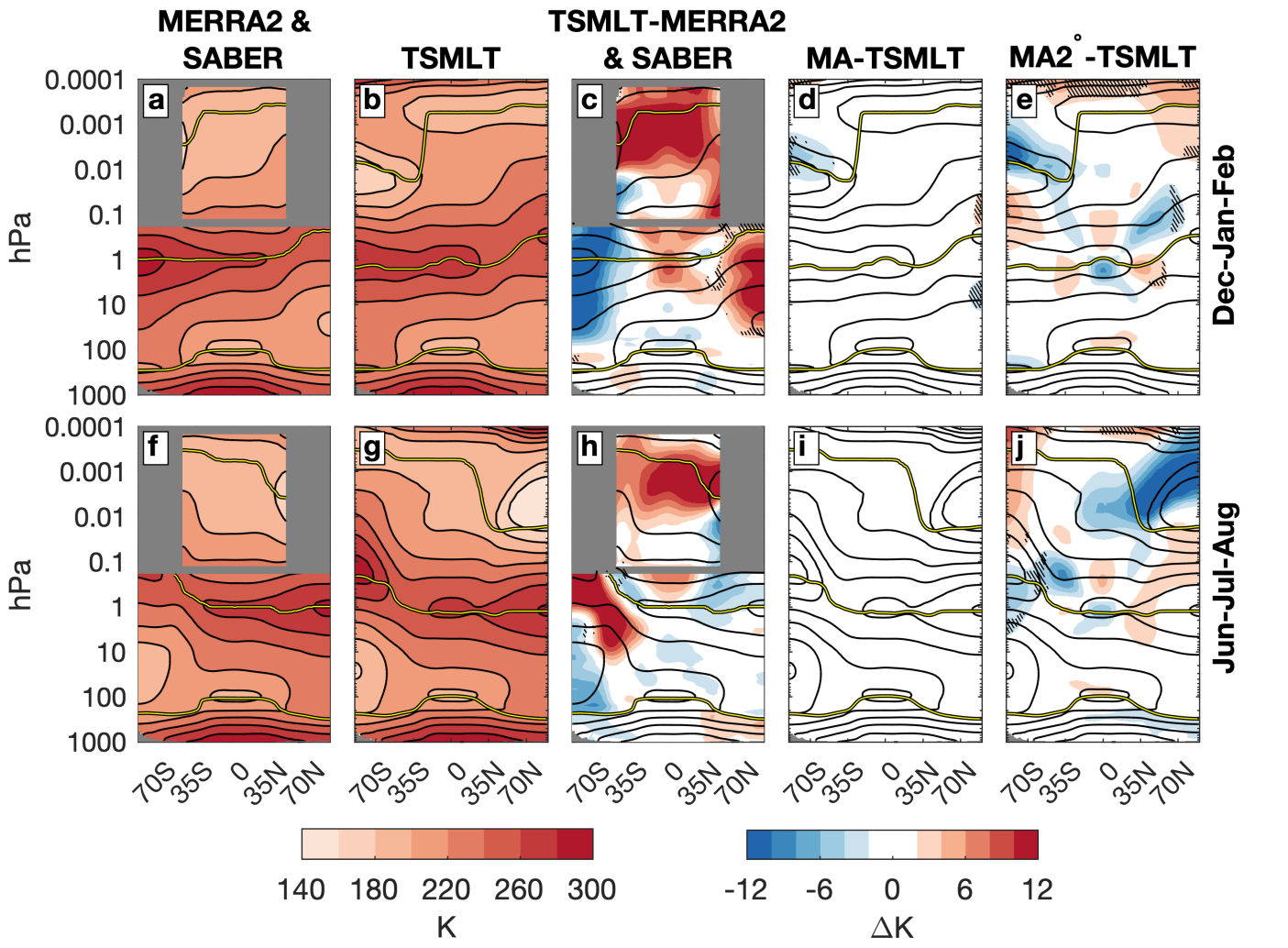
MERRA2 & SABER
TSMLT
TSMLT-MERRA2 & SABER
MA-TSMLT
MA2°-TSMLT
a
b
c
d
e
f
g
h
i
j
hPa
0.0001
0.001
0.01
0.1
1
10
100
1000
Dec-Jan-Feb
Jun-Jul-Aug
70S
35S
0
35N
70N
140
180
220
260
300
K
-12
-6
0
6
12
ΔK

Figure 2.

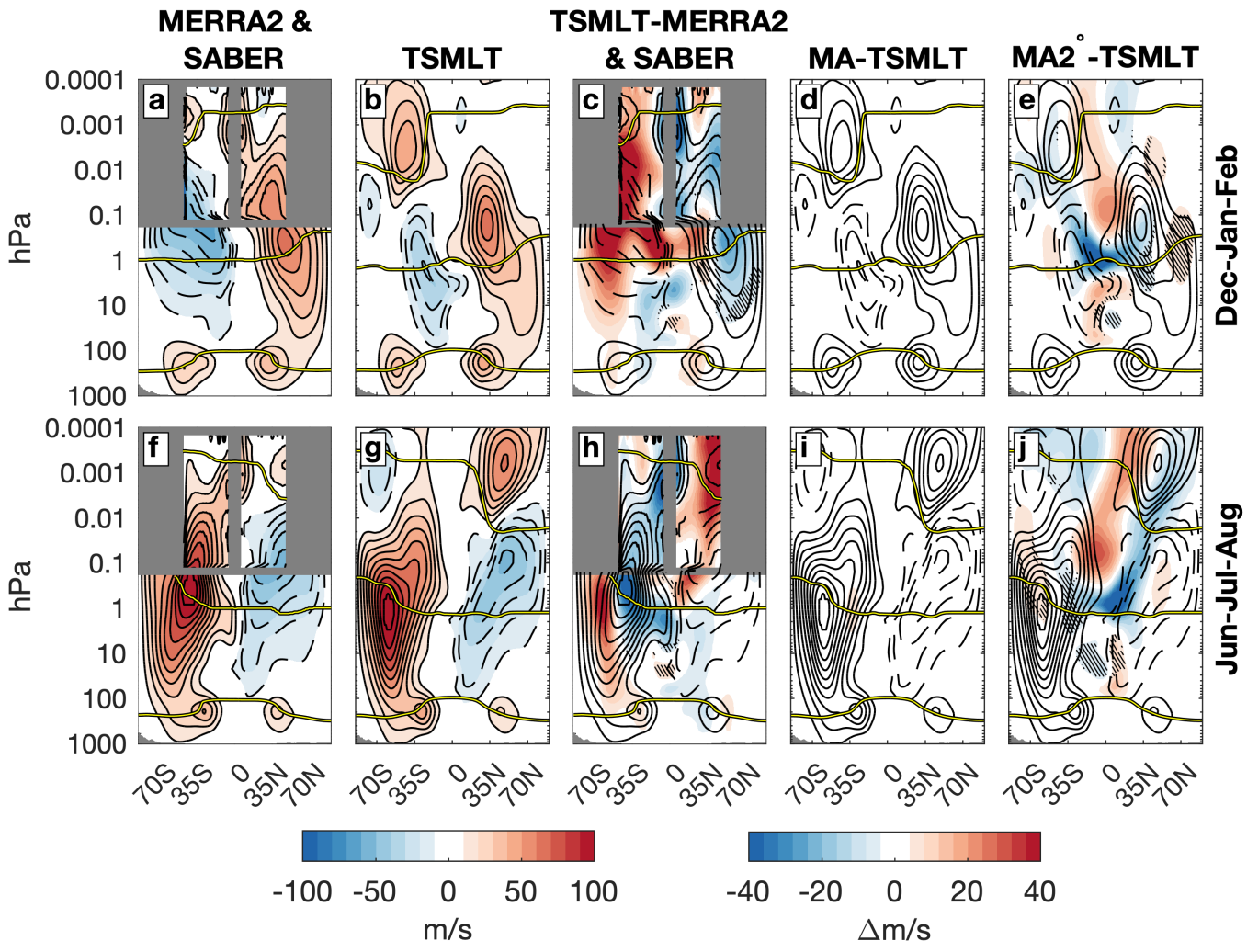
MERRA2 & SABER
TSMLT
TSMLT-MERRA2 & SABER
MA-TSMLT
MA2°-TSMLT
Dec-Jan-Feb
Jun-Jul-Aug
hPa
0.0001
0.001
0.01
0.1
1
10
100
1000
a
b
c
d
e
f
g
h
i
j
70S
35S
0
35N
70N
-100
-50
0
50
100
m/s
-40
-20
0
20
40
Δm/s

Figure 3.

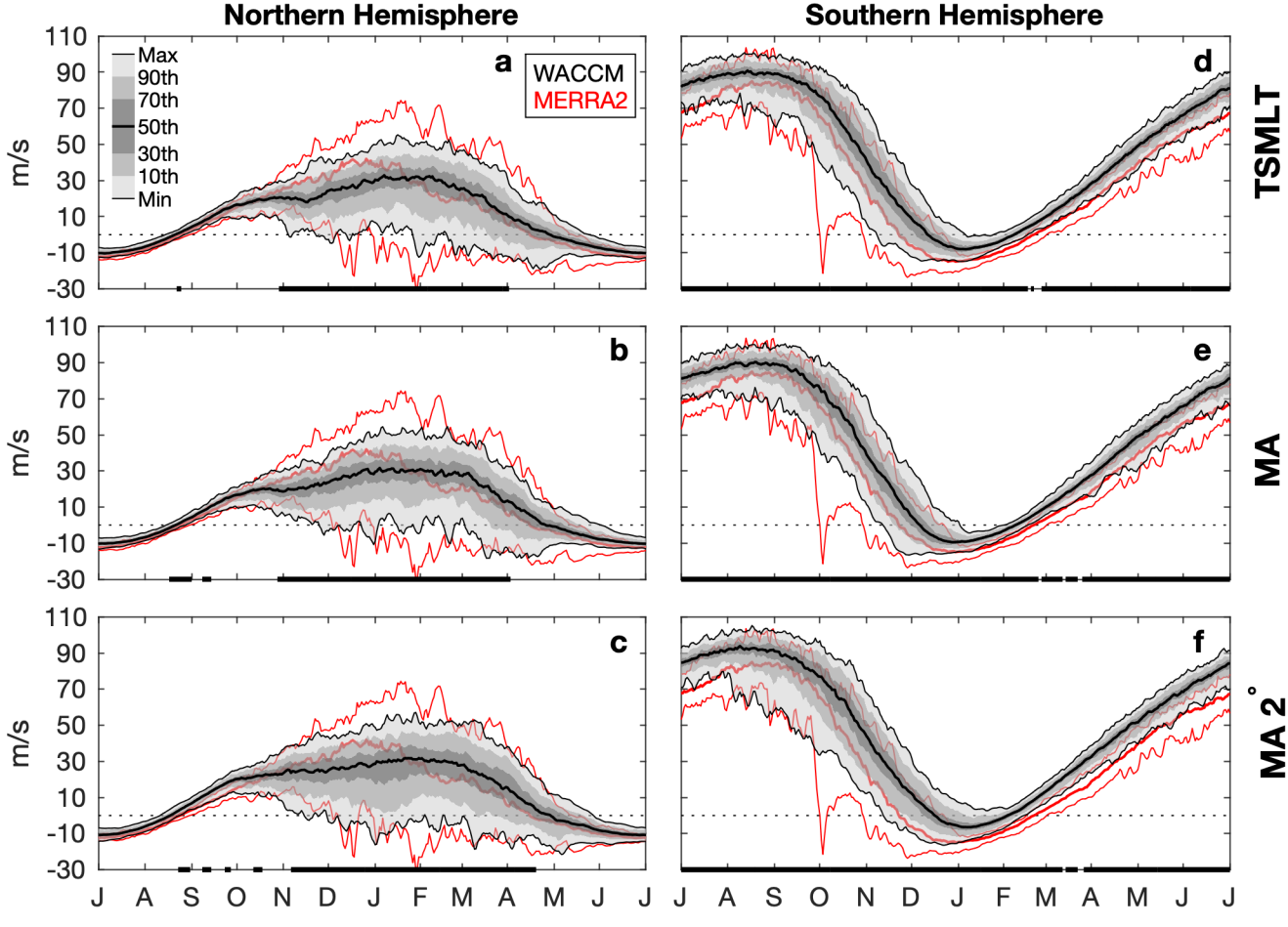
Northern Hemisphere
Southern Hemisphere
Max
90th
70th
50th
30th
10th
Min
WACCM
MERRA2
a
b
c
d
e
f
m/s
110
90
70
50
30
10
-10
-30
TSMLT
MA
MA 2°
J A S O N D J F M A M J J

Figure 4.

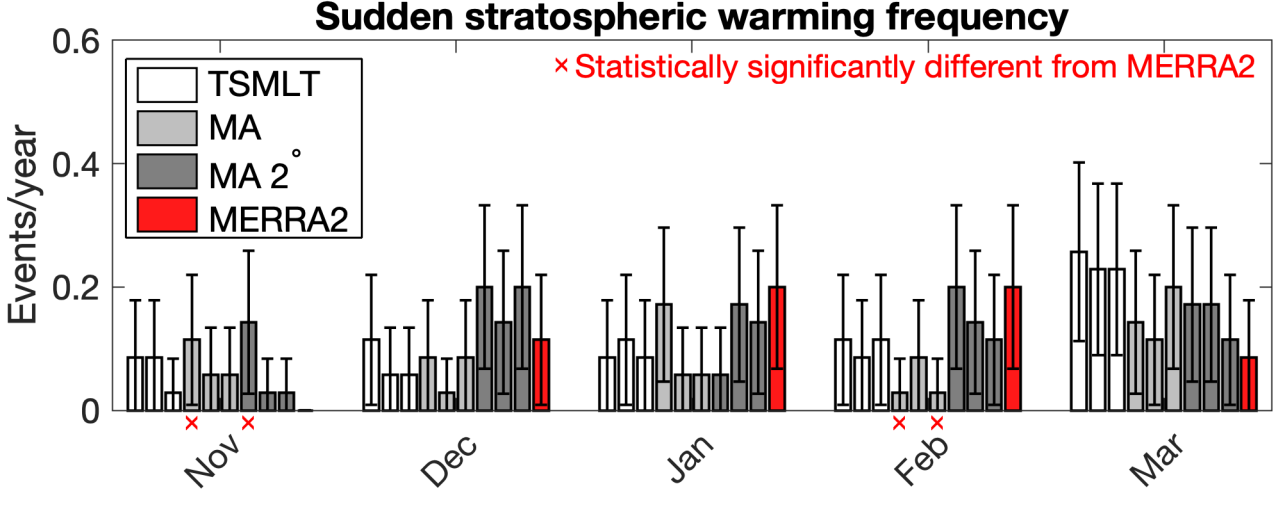
Sudden stratospheric warming frequency
Events/year
0.6
0.4
0.2
0
TSMLT
MA
MA 2°
MERRA2
× Statistically significantly different from MERRA2
Nov
Dec
Jan
Feb
Mar

Figure 5.

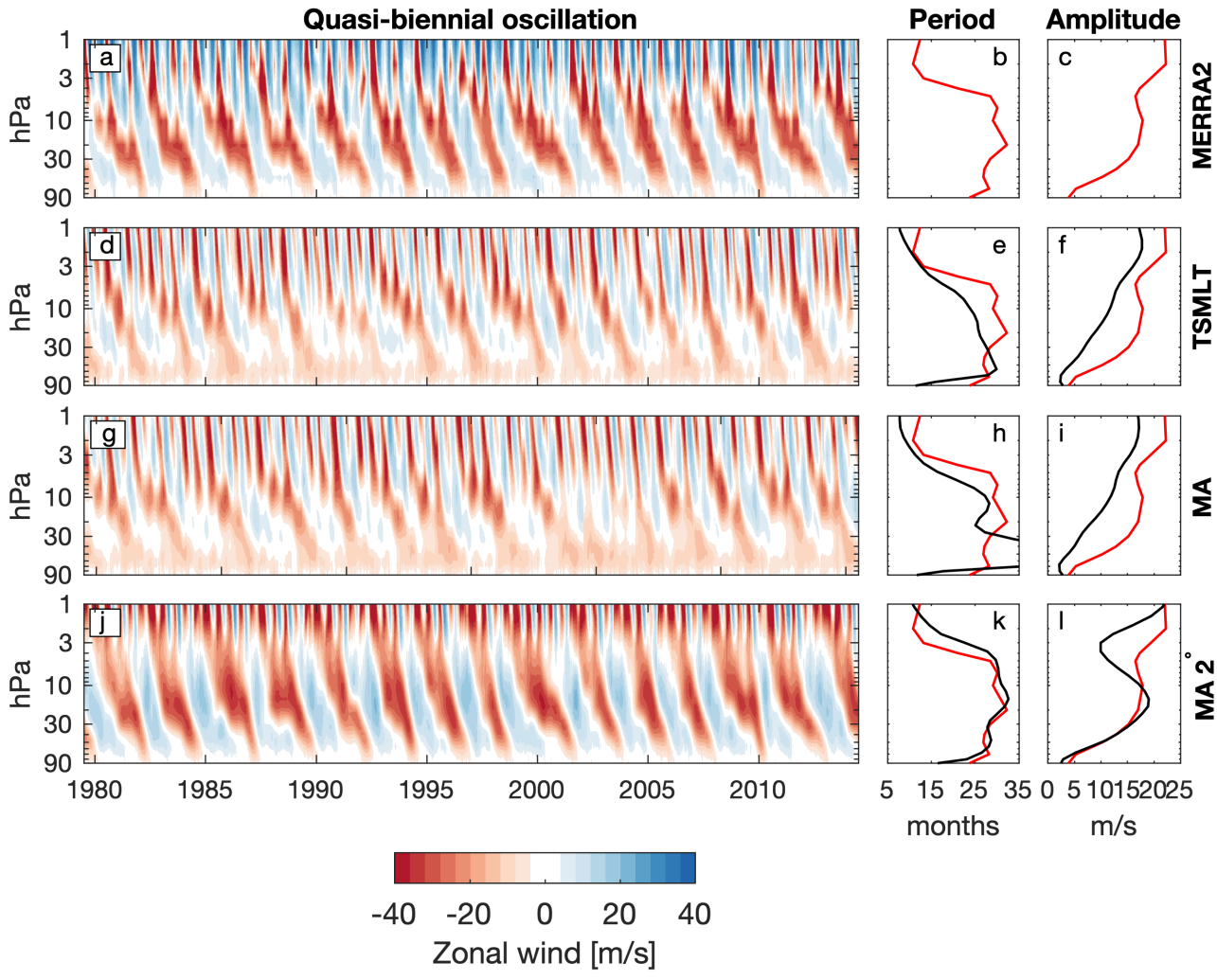
Quasi-biennial oscillation
Period
Amplitude
a
b
c
d
e
f
g
h
i
j
k
l
hPa
1
3
10
30
90
1980
1985
1990
1995
2000
2005
2010
5
15
25
35
months
0
5
10
15
20
25
m/s
MERRA2
TSMLT
MA
MA 2°
-40
-20
0
20
40
Zonal wind [m/s]

Figure 6.

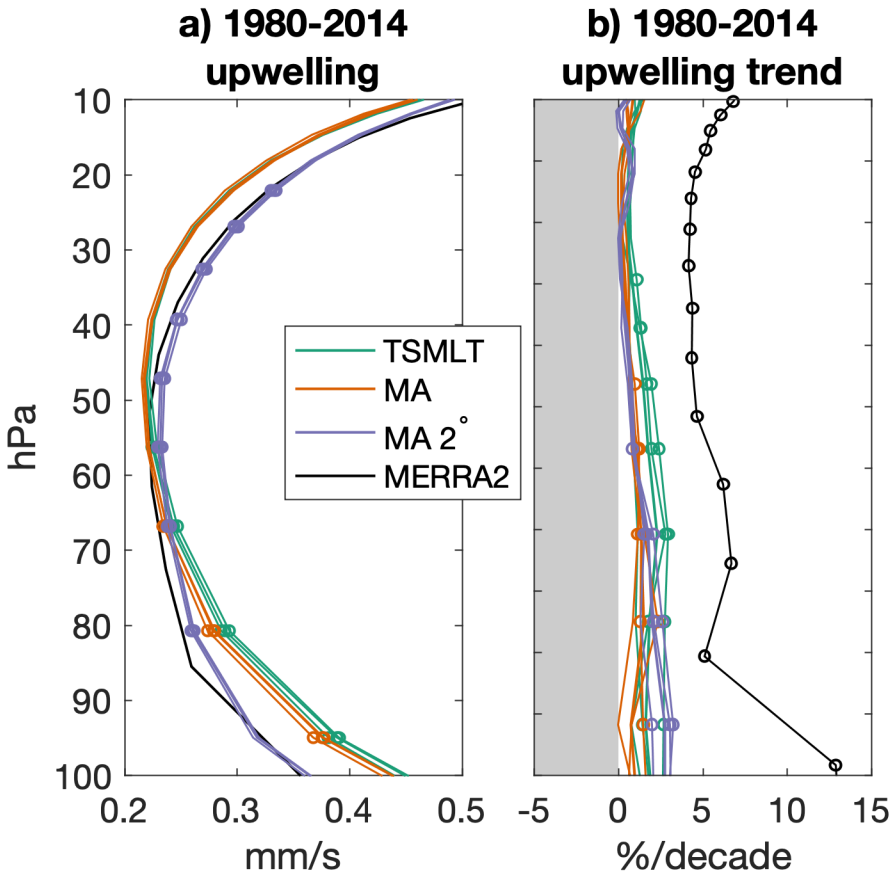
a) 1980-2014
upwelling
b) 1980-2014
upwelling trend
hPa
10
20
30
40
50
60
70
80
90
100
0.2
0.3
0.4
0.5
mm/s
-5
0
5
10
15
%/decade
TSMLT
MA
MA 2°
MERRA2

Figure 7.

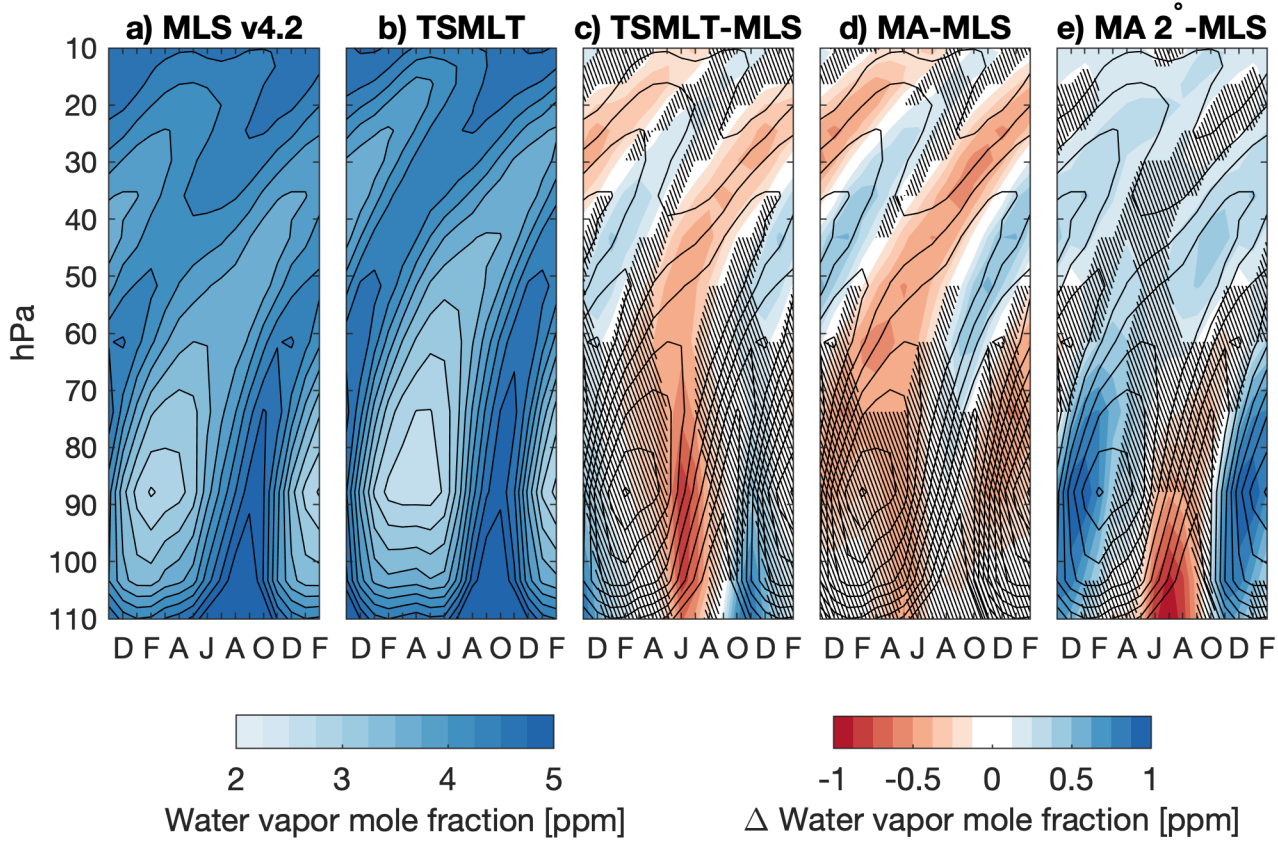
a) MLS v4.2
b) TSMLT
c) TSMLT-MLS
d) MA-MLS
e) MA 2°-MLS
hPa
10
20
30
40
50
60
70
80
90
100
110
D F A J A O D F
2
3
4
5
Water vapor mole fraction [ppm]
-1
-0.5
0
0.5
1
△ Water vapor mole fraction [ppm]

Figure 8.

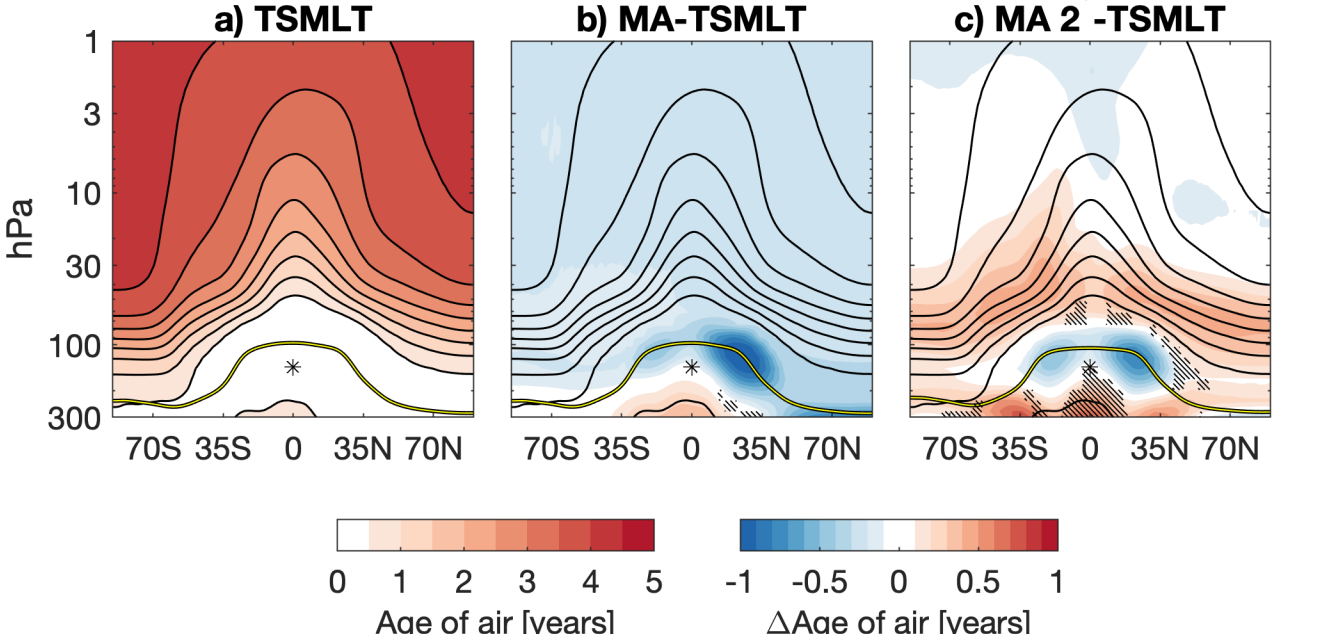
a) TSMLT
b) MA-TSMLT
c) MA 2°-TSMLT
hPa
1
3
10
30
100
300
70S 35S 0 35N 70N
0 1 2 3 4 5
Age of air [years]
-1 -0.5 0 0.5 1
ΔAge of air [years]

Figure 9.

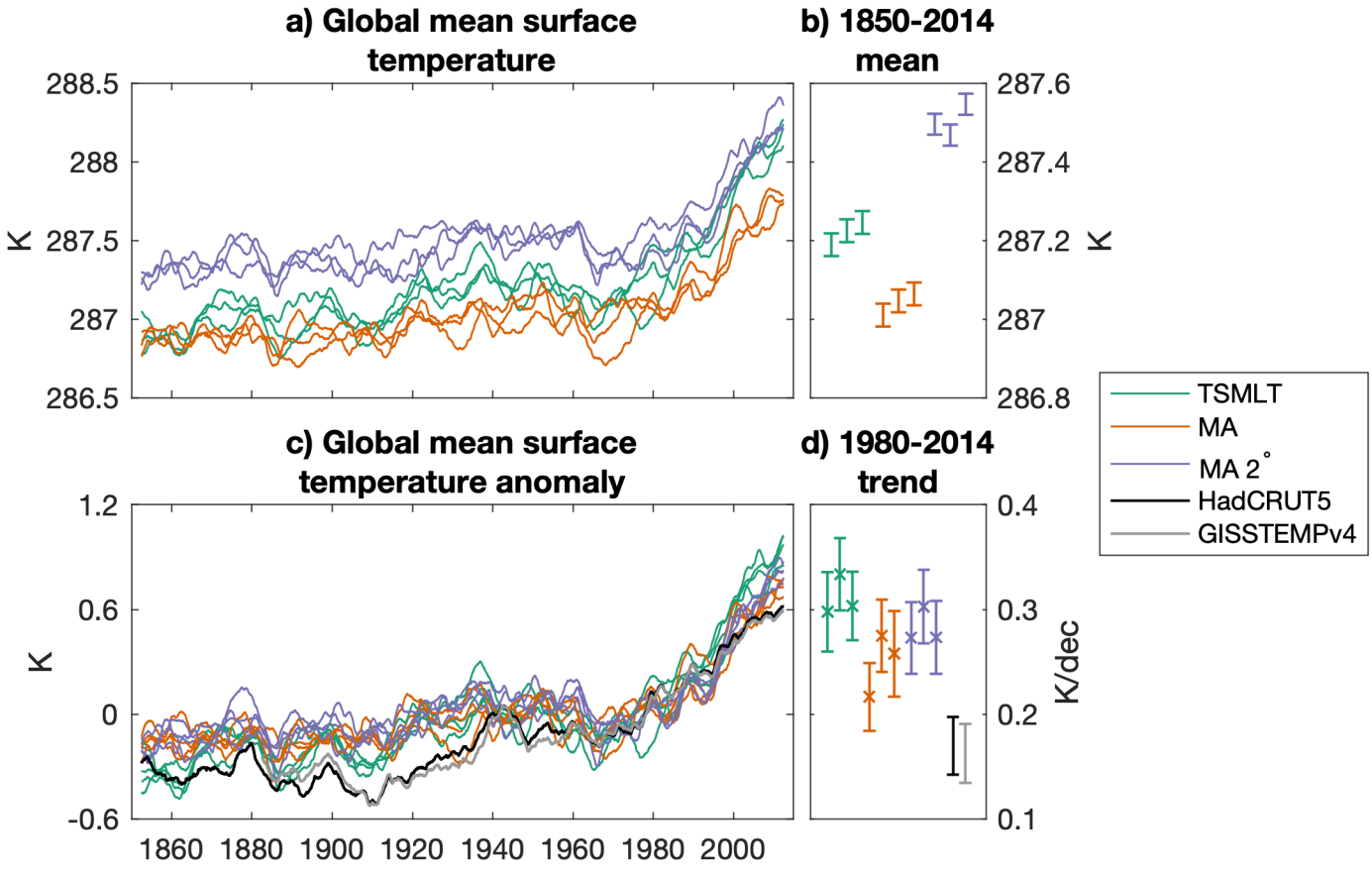
a) Global mean surface temperature
b) 1850-2014 mean
c) Global mean surface temperature anomaly
d) 1980-2014 trend
K
K
K
K/dec
288.5
288
287.5
287
286.5
287.6
287.4
287.2
287
286.8
1.2
0.6
0
-0.6
0.4
0.3
0.2
0.1
1860 1880 1900 1920 1940 1960 1980 2000
TSMLT
MA
MA 2°
HadCRUT5
GISSTEMPv4

Figure 10.

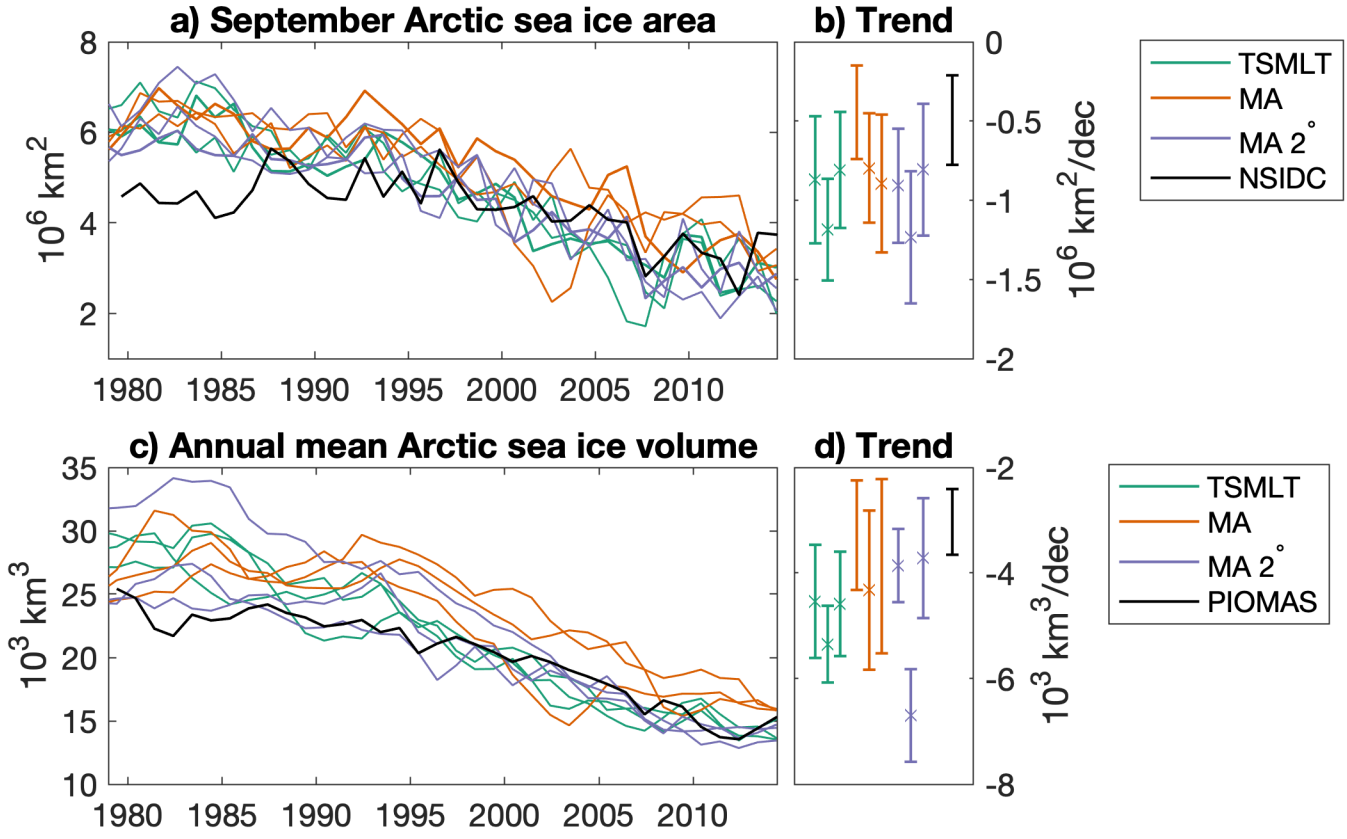
a) September Arctic sea ice area
b) Trend
c) Annual mean Arctic sea ice volume
d) Trend
10^6 km^2
10^6 km^2/dec
10^3 km^3
10^3 km^3/dec
TSMLT
MA
MA 2°
NSIDC
PIOMAS
1980
1985
1990
1995
2000
2005
2010

Figure 11.

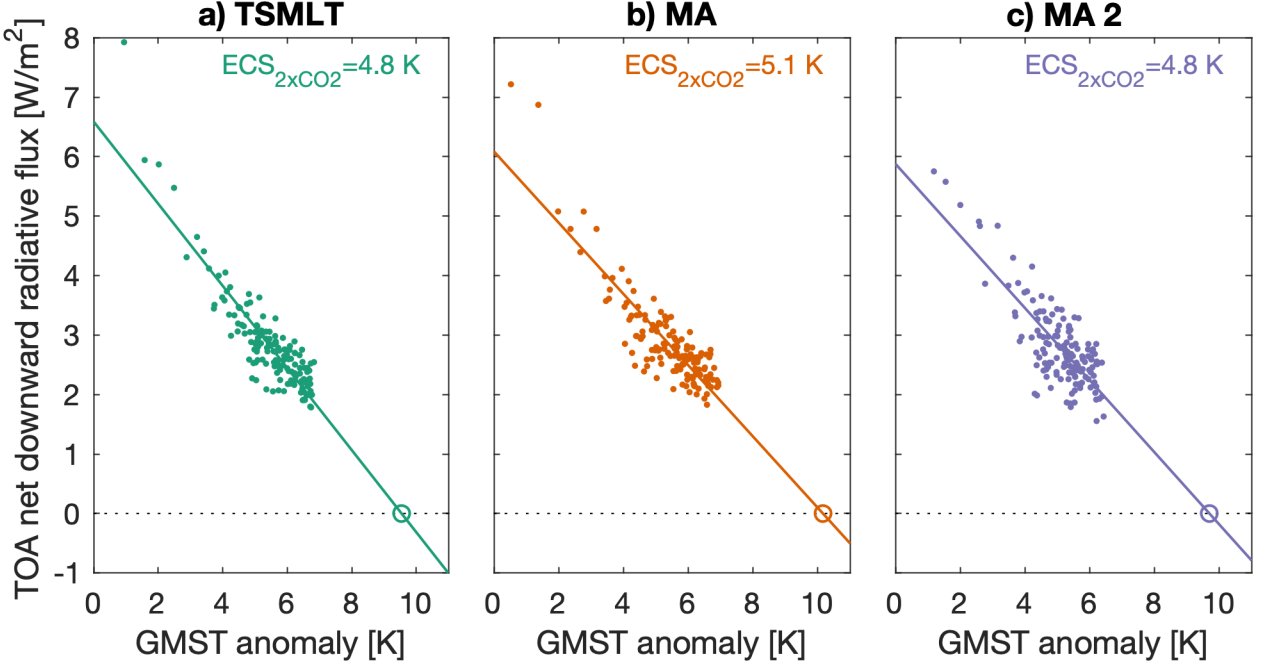
a) TSMLT
b) MA
c) MA 2°
ECS2xCO2=4.8 K
ECS2xCO2=5.1 K
ECS2xCO2=4.8 K
TOA net downward radiative flux [W/m2]
GMST anomaly [K]
GMST anomaly [K]
GMST anomaly [K]
8
7
6
5
4
3
2
1
0
-1
0
2
4
6
8
10

Figure 12.

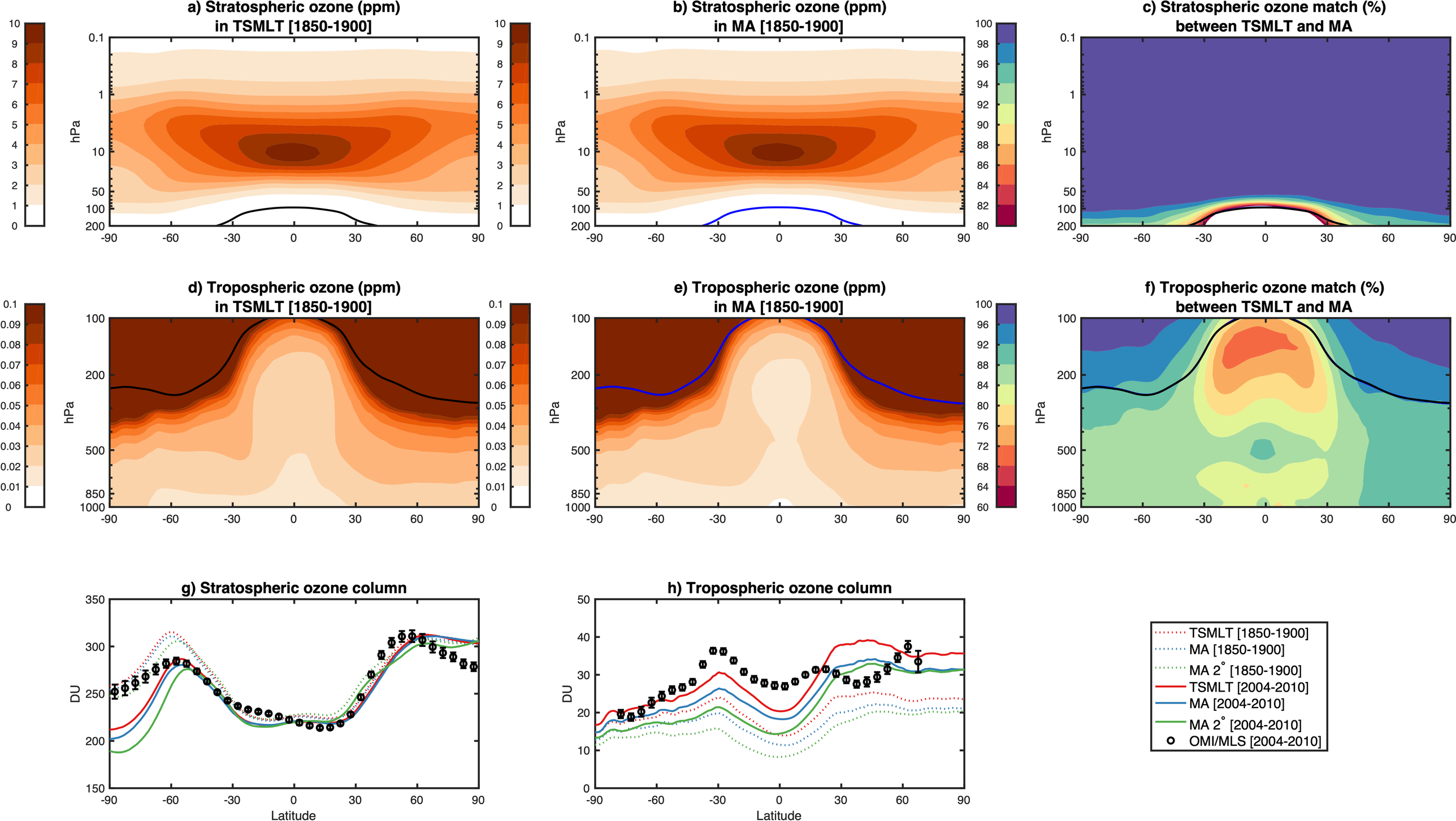
a) Stratospheric ozone (ppm)
in TSMLT [1850-1900]
b) Stratospheric ozone (ppm)
in MA [1850-1900]
c) Stratospheric ozone match (%)
between TSMLT and MA
d) Tropospheric ozone (ppm)
in TSMLT [1850-1900]
e) Tropospheric ozone (ppm)
in MA [1850-1900]
f) Tropospheric ozone match (%)
between TSMLT and MA
g) Stratospheric ozone column
h) Tropospheric ozone column
hPa
DU
Latitude
TSMLT [1850-1900]
MA [1850-1900]
MA 2° [1850-1900]
TSMLT [2004-2010]
MA [2004-2010]
MA 2° [2004-2010]
OMI/MLS [2004-2010]

Figure 13.

Stratospheric ozone evolution (90S-63S, October)

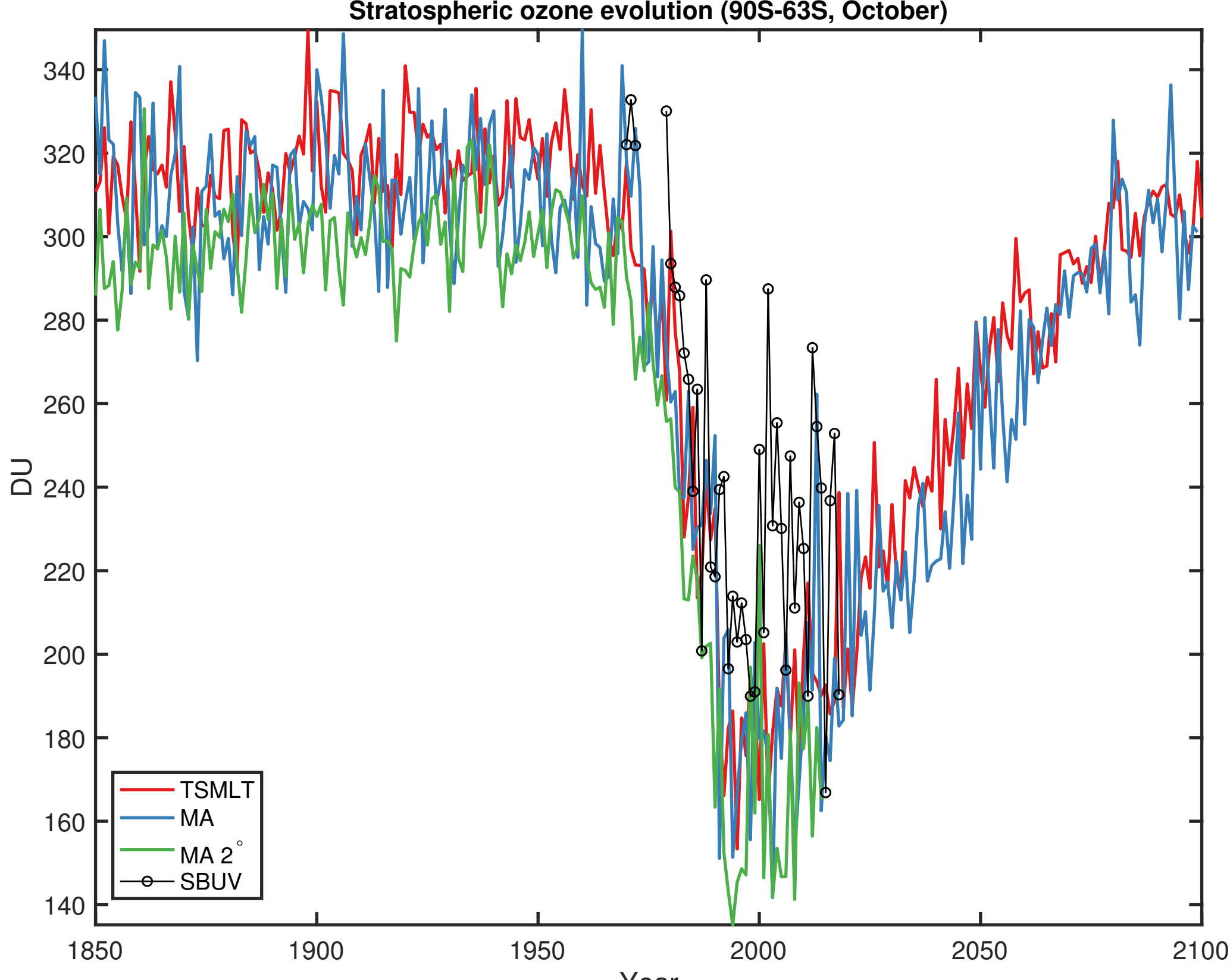

Stratospheric ozone changes compared to 1970-1989 (90S-63S, October)

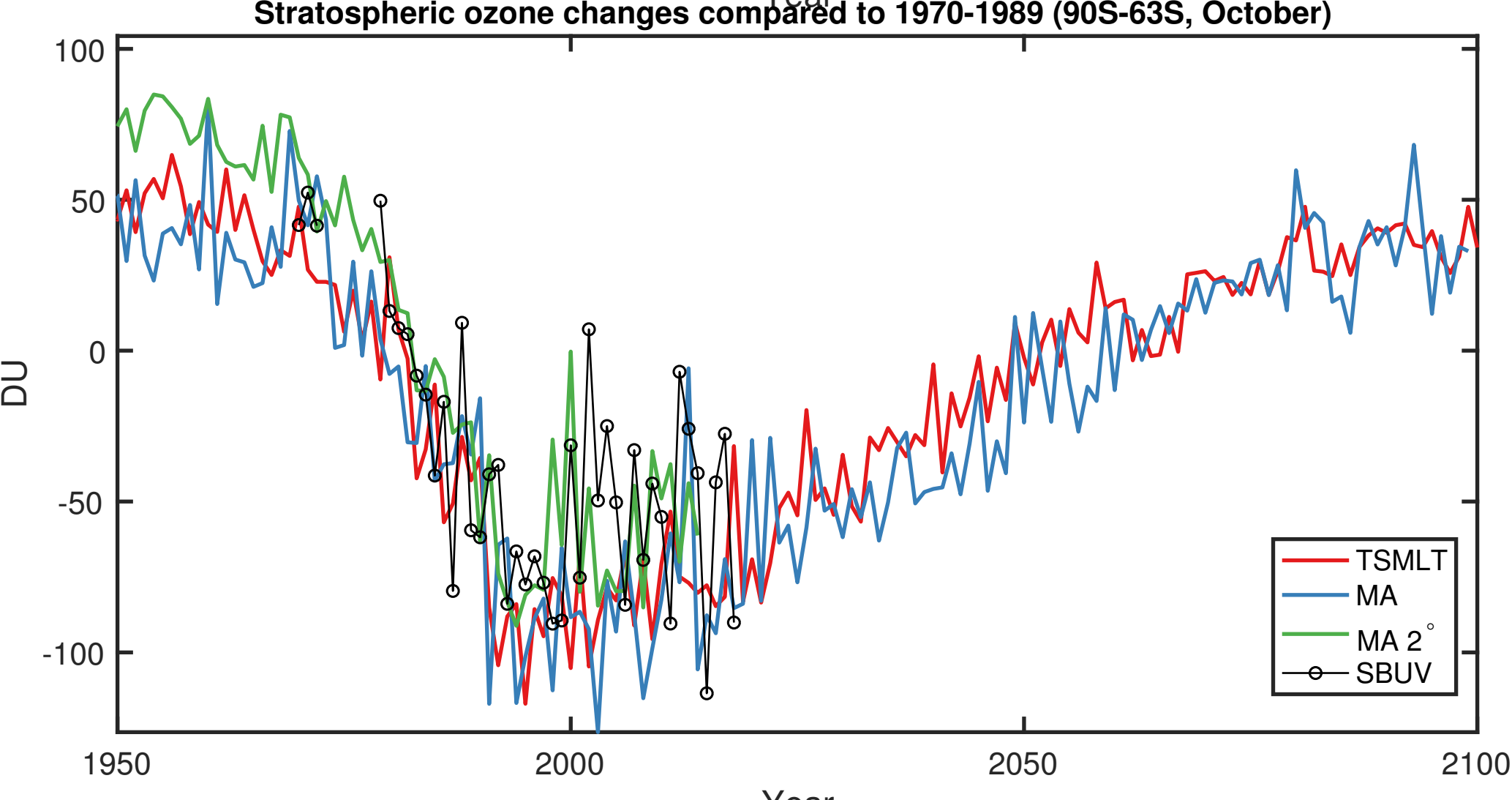

Figure 14.

TSMLT
MA
MA 2°
CMIP6 volcanic aerosol dataset

a) Global stratospheric AOD

AOD

10^{-1}

10^{-2}

1850 1900 1950 2000

b) Global stratospheric AOD changes compared to TSMLT

%

100 50 0

1850 1900 1950 2000

c) Stratospheric AOD without volcanoes [1980-2015]

$\times 10^{-3}$

AOD

12 10 8 6 4 2

-80 -60 -40 -20 0 20 40 60 80

d) Stratospheric AOD after Pinatubo [August 1991-July 1992]

AOD

0.2 0.15 0.1 0.05 0

-80 -60 -40 -20 0 20 40 60 80

Figure 15.

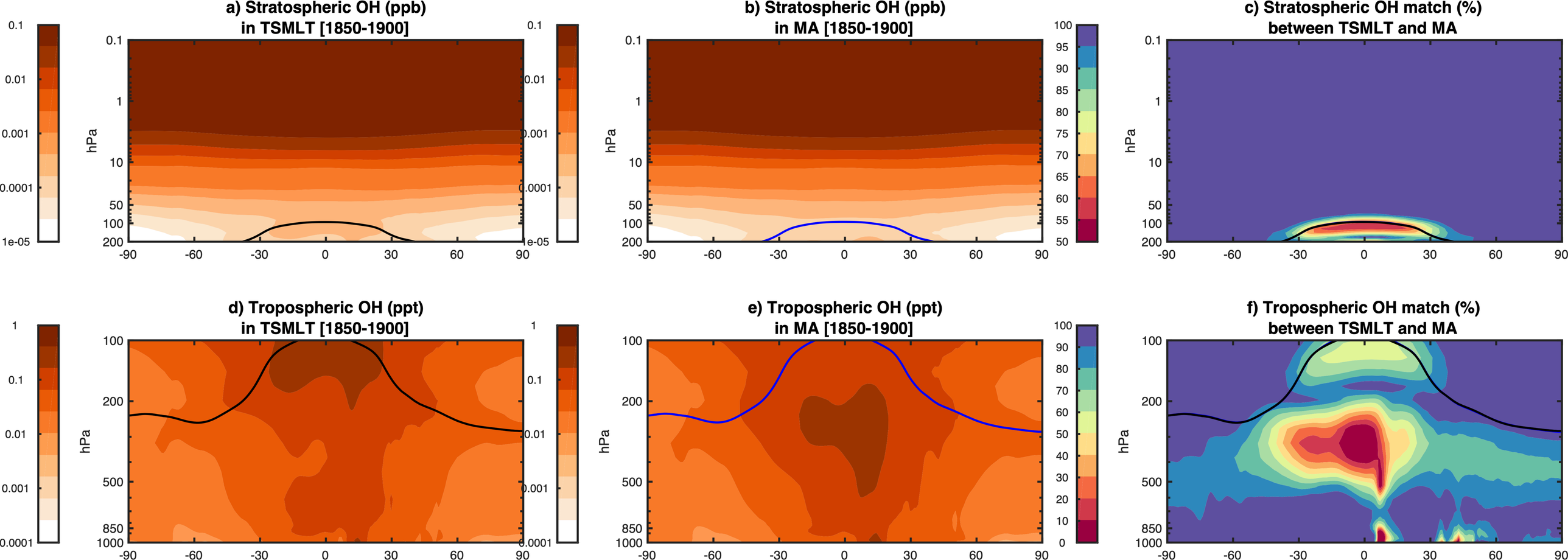
a) Stratospheric OH (ppb)
in TSMLT [1850-1900]
b) Stratospheric OH (ppb)
in MA [1850-1900]
c) Stratospheric OH match (%)
between TSMLT and MA
d) Tropospheric OH (ppt)
in TSMLT [1850-1900]
e) Tropospheric OH (ppt)
in MA [1850-1900]
f) Tropospheric OH match (%)
between TSMLT and MA
hPa
0.1
1
10
50
100
200
500
850
1000
-90
-60
-30
0
30
60
90
0.1
0.01
0.001
0.0001
1e-05
1
100
95
90
85
80
75
70
65
60
55
50
40
30
20
10
0

Figure 16.

a) Global tropospheric AOD

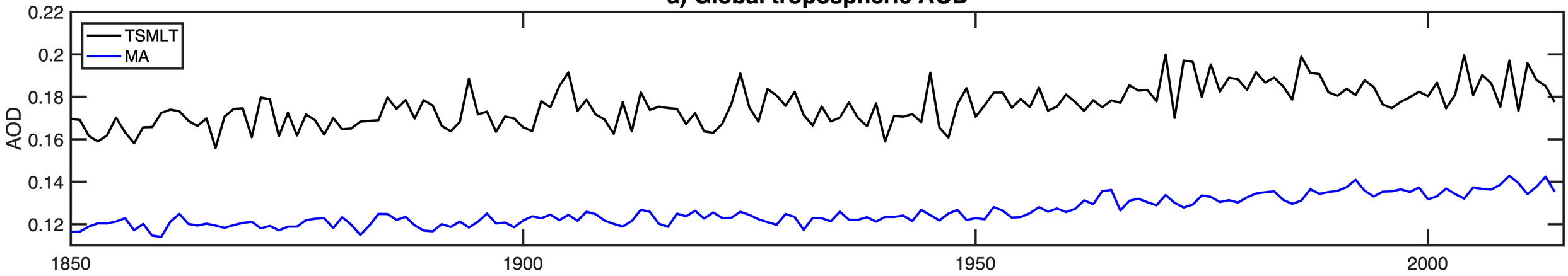

b) Sea Salt (ppb) in TSMLT [1850-2014]

d) Dust (ppb) in TSMLT [1850-2014]

f) Black Carbon (ppt) in TSMLT [1850-2014]

h) POM (ppb) in TSMLT [1850-2014]

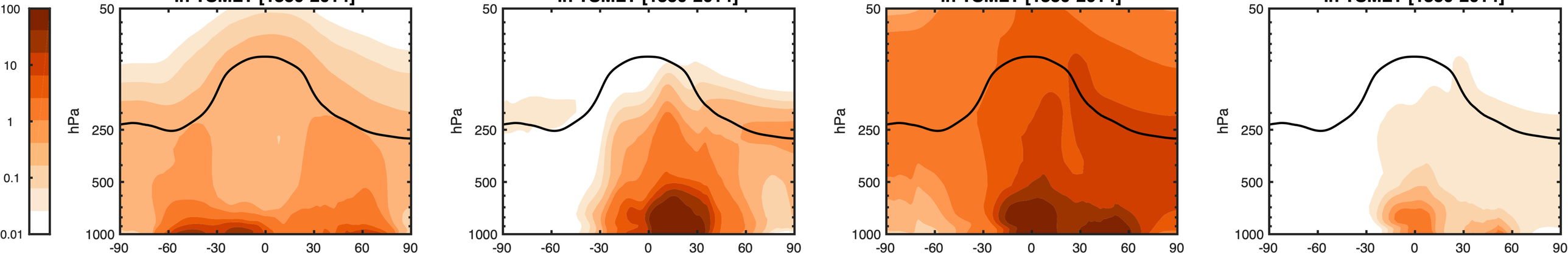

c) Sea Salt match (%) between TSMLT and MA

e) Dust match (%) between TSMLT and MA

g) Black carbon match (%) between TSMLT and MA

i) POM match (%) between TSMLT and MA